Estimation of Vertical Heat Diffusivity at the Base of the Mixed Layer in the Bay of Bengal

M. S. Girishkumar[1] [iD], **K. Ashin[1]**, **M. J. McPhaden[2]** [iD], **B. Balaji[1,3]**, and **B. Praveenkumar[1]**

[1]Indian National Centre for Ocean Information Services, Hyderabad, India, [2]Pacific Marine Environmental Laboratory, National Oceanic and Atmospheric Administration, Seattle, WA, USA, [3]Indian Institute of Tropical Meteorology, Pashan, Pune, India

Abstract One approach to estimating vertical heat diffusivity (K_T) is to compute it from the residual of the mixed layer (ML) heat budget. Based on this approach, we use moored buoy data at 15°N, 12°N, and 8°N along 90°E over the period of 2007–2018 to estimate the seasonal average of K_T at the base of the mixed layer in the Bay of Bengal (BoB). We find that K_T is lower during spring and higher during winter compared to summer and fall at the mooring locations. Moreover, K_T is generally higher in the southern BoB compared to the northern BoB. The present study also shows that the seasonal and spatial variability of K_T is modulated both by stratification at the base of ML and by seasonal and spatial heterogeneity in atmospheric forcing, most notably wind stress and buoyancy flux. The availability of information on the spatial and seasonal variability of K_T in the BoB will facilitate evaluation and validation of turbulent mixing parameterization schemes incorporated into ocean models.

1. Introduction

The Bay of Bengal (BoB) is a semienclosed basin in the northern Indian Ocean, forced locally by the seasonal reversal of monsoon winds and remotely through eastward propagating planetary waves that are triggered by winds in the equatorial Indian Ocean (Shankar et al., 2002). In addition, due to the large influx of river water and excess precipitation over evaporation, the near-surface water is less saline, which leads to the BoB being one of the freshest oceanic basins in the tropical oceans (Varkey et al., 1996). The presence of surface fresh water above subsurface high saline water supports a strong halocline which then leads to the formation of strong barrier layers (BLs), the layer between the base of the mixed layer (ML), and the top of the thermocline (Girishkumar et al., 2011; Rao & Sivakumar, 2003; Thadathil et al., 2007).

The presence of temperature inversions is common in these BLs which isolate the surface ML from the cold thermocline water beneath (Girishkumar et al., 2011;Girishkumar, Ravichandran, & McPhaden, 2013; Rao & Sivakumar, 2003; Thadathil et al., 2002; Thadathil et al., 2007; Thangaprakash et al., 2016; Thadathil et al., 2016). The presence of BLs and temperature inversions plays a significant role in the seasonal evolution of sea surface temperature (SST) in the BoB (Rao & Sivakumar, 2003; Girishkumar et al., 2011; Girishkumar, Ravichandran, & McPhaden, 2013; Girishkumar et al., 2017; Thangaprakash et al., 2016). The relative contribution of various processes that modulate SST evolution on seasonal, intraseasonal, and interannual time scales have been examined by several earlier studies (Girishkumar et al., 2011; Girishkumar, Ravichandran, & McPhaden, 2013; Girishkumar et al., 2017; Rao & Sivakumar, 2003; Thadathil et al., 2002; Thadathil et al., 2007; Thadathil et al., 2016; Thangaprakash et al., 2016; Warner et al., 2016). These studies suggest that net surface heat flux dominates processes that modulate SST in the BoB (Girishkumar, Ravichandran, & McPhaden, 2013; Girishkumar et al., 2017; Prasad, 2004; Rao & Sivakumar, 2000; Sengupta et al., 2002; Shenoi et al., 2002; Thadathil et al., 2016; Thangaprakash et al., 2016) but that entrainment cooling at the base of ML at times also plays an important role (Girishkumar, Ravichandran, & McPhaden, 2013; Girishkumar et al., 2017; Prasad, 2004; Rao & Sivakumar, 2000; Sengupta et al., 2002; Thadathil et al., 2016; Thangaprakash et al., 2016).

Vertical turbulent mixing due to entrainment and diffusive heat flux at the base of ML are important processes that help to determine the ML heat budget. Both entrainment and vertical diffusive mixing are turbulent processes, whose evolution depends on upper-ocean structure and time evolution of the forcing. In this study, we are specifically interested in estimating vertical diffusive mixing as distinct of entrainment. In a

stratified ocean, vertical diffusive heat flux below the base of the ML can be expressed as $-\rho C_p K_T \partial T/\partial Z$, where ρ is the density of seawater, C_p is specific heat capacity of seawater, K_T is the vertical heat diffusivity, and $\partial T/\partial Z$ is the average temperature gradient between the base of ML to a certain depth below the ML. Accurate estimation of vertical diffusive heat flux and vertical heat diffusivity at the base of ML can be achieved through temperature microstructure measurements (Warner et al., 2016, hereafter W16; Cronin et al., 2015; Lucas et al., 2016; Shroyer et al., 2016). Such measurements are primarily made through ship-board observations, and they are relatively sparse in both space and time. Further, these studies have reported distinct seasonal and spatial variability of vertical diffusive heat fluxes at the base of ML (W16; Cronin et al., 2015; Hummels et al., 2013). Recently, there were a few efforts to equip microstructure temperature sensors on the moorings to document the seasonal variability of upper-ocean vertical diffusive heat flux (Moum et al., 2013; W16). These studies documented the seasonal variability of subsurface vertical heat diffusivity and highlighted the importance of vertical diffusive heat flux in the near-surface layer and its influence on seasonal and intraseasonal SST variability. For example, year-long (December 2013 to November, 2014) microstructure temperature measurements at 15 m depth from a Research Moored Array for African-Asian-Australian Monsoon Analysis and Prediction (RAMA) moored buoy at12°N, 90°E in the BoB (McPhaden et al., 2009) show that the seasonal average of subsurface vertical diffusive heat fluxes between winter ($-7\,\mathrm{W\,m^{-2}}$) and summer ($-22\,\mathrm{W\,m^{-2}}$) are significantly different (W16). Thus, moored buoy microstructure measurements at fixed depths can provide continuous long-term observations, but temperature microstructure sensors deployed at a relatively small number of fixed depths may lead to biased estimates of K_T with respect to the base of ML, which can undergo large vertical excursions.

An alternate approach to estimating the vertical diffusivity of heat is through a ML heat budget residual method (Bond & McPhaden, 1995; Cronin et al., 2015; de Boisseson et al., 2010; Foltz et al., 2010; Kolodziejczyk & Gaillard, 2013; Wade et al., 2011; Wang & McPhaden, 1999). Cronin et al. (2015) extended these efforts further with a detailed discussion of different selection criteria to estimate the vertical heat diffusivity at the base of ML. Following Cronin et al. (2015), our goal is to estimate the seasonal average of vertical heat diffusivity at the base of ML at RAMA mooring locations in the BoB. In this study, we assume isopycnals are flat at the mooring locations so that diapycnal heat flux is equivalent to vertical diffusive heat flux.

We start with 12°N, 90°E RAMA mooring, where W16 has already documented the seasonal median of vertical heat diffusivity at 15 m depth using microstructure measurements. This site provides a unique opportunity to compare and validate the estimation of vertical heat diffusivity based on a ML heat budget approach. We will show that our estimation of vertical heat diffusivity based on the ML heat budget after applying certain filtering criterion is in good agreement with respect to W16, which gives us confidence to extend the analysis to two other RAMA mooring locations (8°N, 90°E and 15°N, 90°E) in the BoB.

This paper is organized as follows. The data set used and methodology followed is described in section 2. The computation of the vertical heat diffusivity estimated from the residual of the ML heat budget at the 12°N, 90°E RAMA buoy location and its comparison with W16 results is described in section 3. In section 3 we also extend our analysis to other mooring locations in the BoB. The results are summarized and discussed in section 4.

2. Data and Methods

In this study we used data from RAMA moorings at 8°N, 90°E for 2007–2018 and at 12N, 90E and 15N and 90E for 2008–2018 (Figure 1) (McPhaden et al., 2009). RAMA buoys provide daily time series of temperature at depths of 1, 5, 10, 20, 40, 60, 80, 100, 120, 140, 180, 300, and 500 m and salinity at depths of 1, 5, 10, 20, 40, 60, and 100 m. The 1 m value of temperature we nominally refer to as SST. In addition, on the surface buoy, air temperature and relative humidity are measured at 3 m height, wind speed and direction at 4 m height, and shortwave radiation at 3.5 m height. Downwelling longwave radiation is also directly measured at 3.5 m height on the 15°N buoy but not the other mooring sites (McPhaden et al., 2009).

Optimal interpolated (OI) Tropical Rainfall Measuring Mission (TRMM) Microwave Imager (TMI) + Advanced Microwave Scanning Radiometer for the for the Earth Observing System (AMSR-E) SST product (OI-SST) data are used to describe the seasonal variability of SST in the BoB (Gentemann
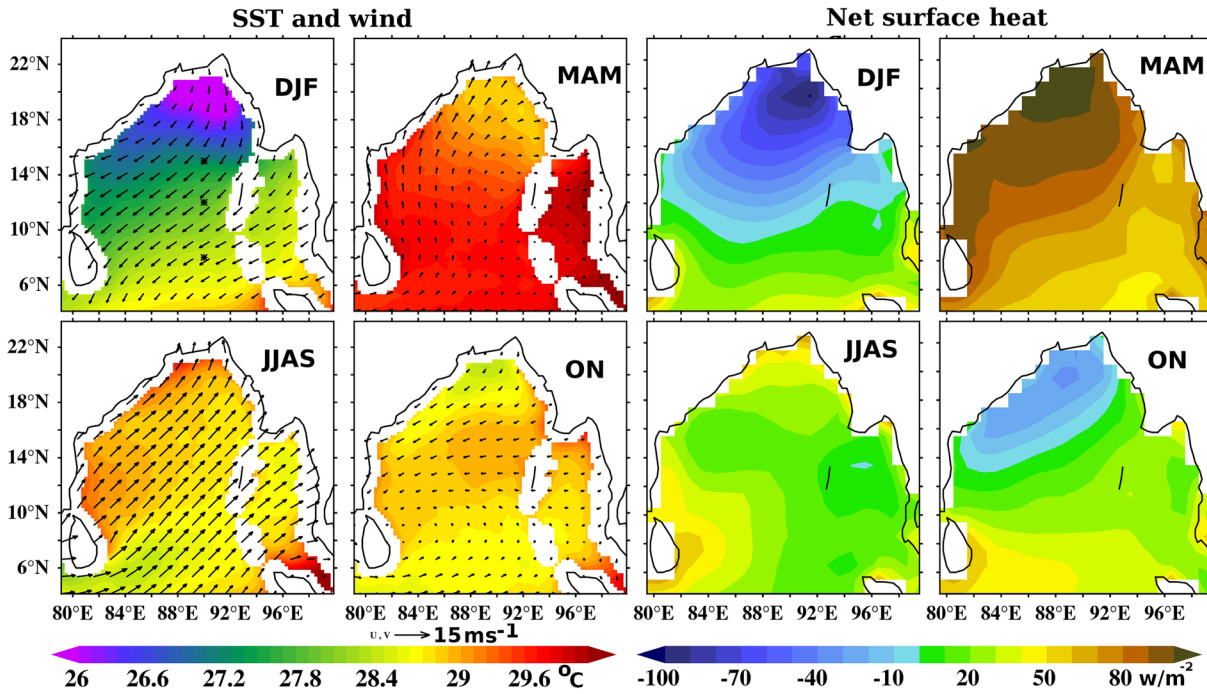
Figure 1. The climatological average of microwave OI-SST (°C; 1998–2017) and ASCAT wind vector (m s^{-1}; 2007–2017) and TropFlux total surface heat flux (W m^{-2}; 1992–2017; sum of net shortwave radiation, net longwave radiation, and latent and sensible heat flux) during four different seasons (spring: March–May, summer: June–September, fall: October–November, and winter: December–February). The RAMA mooring locations (8°N, 12°N, and 15°N along 90°E) in the BoB are marked in pink circles.

et al., 2004). Advanced Scatterometer (ASCAT) (2009–2016) wind vector data are used to explain seasonal variability of near-surface atmospheric circulation in the BoB (Ricciardulli & Wentz, 2016). TropFlux total surface heat flux (sum of net shortwave radiation, net longwave radiation, and latent and sensible heat flux) data are used to describe the modulation of net surface heat flux on seasonal time scales in the BoB (Praveen Kumar et al., 2012).

ML depth (MLD) is defined as the depth where the density changes by 0.125 kg m^{-3} with respect to surface density. This equates to a temperature difference of 0.4 °C in the absence of any salinity stratification for typical upper-ocean salinity and temperature in the BoB. Hence, consistent with the density criterion, the isothermal layer depth (ILD) is defined as the depth where the temperature is 0.4 °C lower than SST. The difference between ILD and MLD is defined as BL thickness (BLT) (Girishkumar et al., 2017).

The ML heat budget is examined using the expression given by Girishkumar et al. (2017)

$$\underbrace{\rho C_p h \frac{\partial T}{\partial t}}_{(a)} = \underbrace{\left(Q_{\text{net}} - Q_{\text{pen}} \right)}_{(b)} - \underbrace{\rho C_p h \left[u \frac{\partial T}{\partial x} + v \frac{\partial T}{\partial y} \right]}_{(c)} - \underbrace{\rho C_p h H \left[W_h + \frac{\partial h}{\partial t} \right] \frac{(T - T_h)}{h}}_{(d)} + \underbrace{\text{Residual}}_{(e)} \tag{1}$$

The individual terms in equation 1 represent (a) ML heat storage rate as defined in Moisin and Niiler (1998) (b) net surface heat flux, (c) horizontal advection, (d) vertical processes (sum of entrainment and vertical advection), and (e) residual. T is temperature averaged over ML, t is time, ρ is the density of seawater, C_p is specific heat capacity of seawater, h is MLD, and T_h is the temperature of water entrained into the ML, taken to be temperature at 5 m below the MLD. Vertical advection below the ML (W_h; m day^{-1}) is inferred from the rate of change of isotherm in the thermocline McPhaden (1982). The vertical profile of RAMA temperature data shows the strongest vertical temperature gradient (approximately 0.18 to 0.26 °C m^{-1}) is found around the depth of 23 °C isotherm (D23; marked as thick black lines) (Figure 2). Thus, we use D23 as representative of thermocline depth in the BoB in this study, consistent with an earlier study in the BoB (Girishkumar, Ravichandran, & Han, 2013), and estimate W_h (equation 1) from its time derivative. The
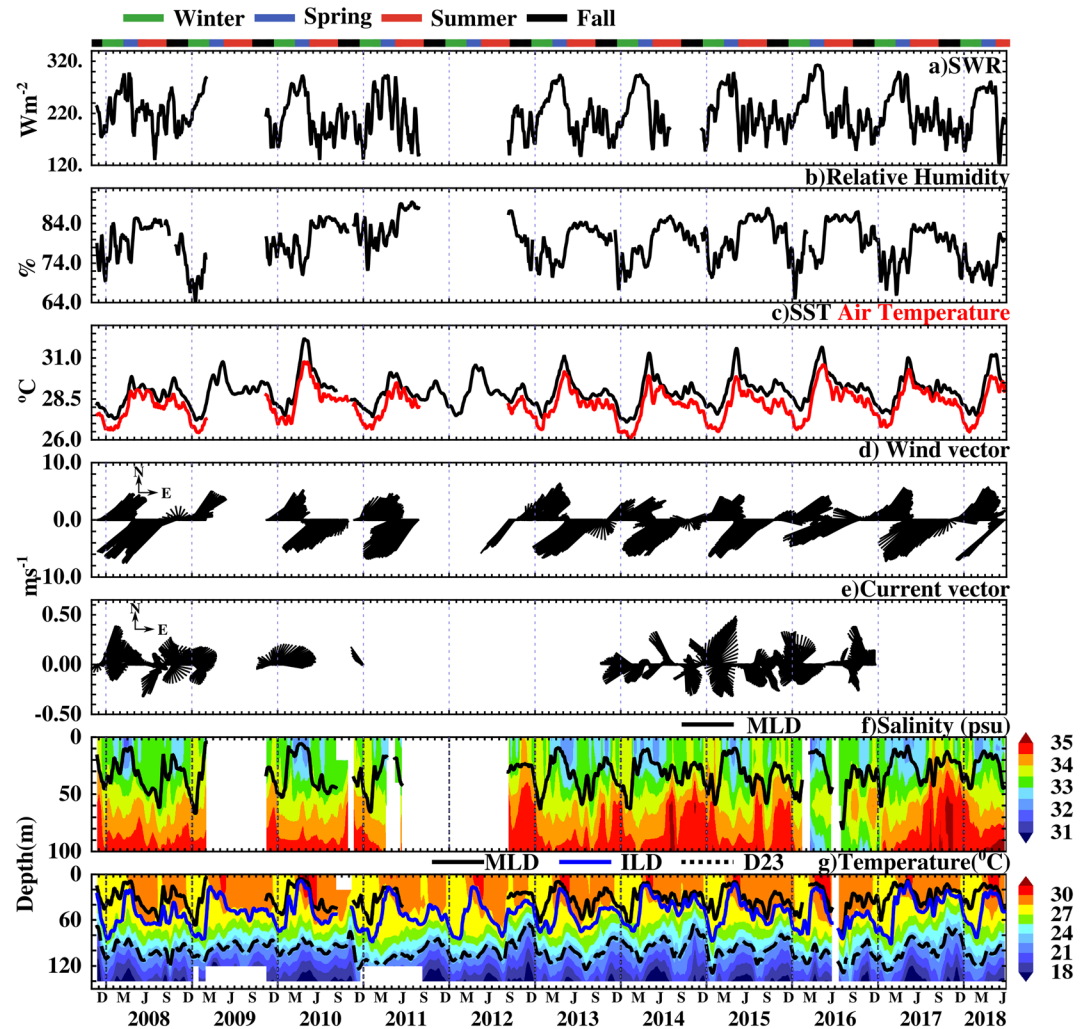
Figure 2. Daily time series of (a) net shortwave radiation (W m^{-2}), (b) relative humidity (%), (c) air temperature (red line; °C) and SST (black line; °C), (d) wind velocity vectors (m s^{-1}), (e) current velocity vectors (m s^{-1}), (f) salinity (psu), and (g) temperature (°C) obtained from RAMA mooring at 12°N, 90°E in the BoB. The MLD (m), ILD (m), and D23 (m) are marked as a thick black line, thick blue line, and thick dashed line, respectively, in panel (g). Thick black line in panel (f) represents MLD (m). A 15 day running mean is applied to all data for better representations. The black dashed vertical line represents annual boundaries. The color bar above the figure represents the seasonal boundaries (green = winter, blue = spring, red = summer and black = fall).

rate of change in MLD is $\partial h/\partial t$ (m day^{-1}), and H is the Heaviside step function [=0 if $(W_h + \partial h/\partial t) < 0$ and = 1 if $(W_h + \partial h/\partial t) > 0$] (Girishkumar et al., 2017), which indicates that entrainment can change ML temperature but detrainment due to restratification in principle does not.

The net surface heat flux term (Q_{net}) is the sum of net shortwave radiation (Q_{sw}) minus penetrative shortwave radiation (Q_{pen}), net longwave radiation (Q_{lw}), latent heat flux (Q_{lat}), and sensible (Q_{sen}) heat flux. Latent (Q_{lat}) and sensible (Q_{sen}) heat fluxes are estimated using SST (1 m), air temperature, relative humidity, and wind speed from the mooring using Coupled Ocean-Atmosphere Response Experiment (COARE 3.0b) bulk flux algorithm (Fairall et al., 2003). The downwelling shortwave radiation obtained from the mooring is corrected for albedo to estimate net shortwave radiation (downwelling short wave radiation × 0.945). At 15°N, the net longwave radiation is estimated using measured downwelling longwave radiation following the methodology of Dickey et al. (1994). The RAMA moorings at 8°N and 12°N do not provide longwave radiation. Hence, we used net longwave radiation from TropFlux to facilitate the analysis (Praveen Kumar et al., 2012).

Following Morel and Antoine (1994), the penetrative shortwave radiation (Q_{pen}) below the ML is estimated by $Q_{\text{pen}} = 0.47 Q_{\text{Shortwave}} \left[V_1 e^{-h/\xi_1} + V_2 e^{-h/\xi_2} \right]$, where h is the MLD. The parameter ζ_1 is the attenuation depth for the red part of visible spectrum and ζ_2 is the attenuation depth for the blue part of visible spectrum and ultraviolet radiation. Following Foltz and McPhaden (2005) we have chosen 0.47 for the fraction of solar radiation that is not absorbed in the upper 1–2 m of water column and therefore capable of penetrating though the base of the mixed layer. The values of V_1, V_2, ζ_1, and ζ_2 are estimated from chlorophyll-a (mg m^{-3}) data using the method from Morel and Antoine (1994), with the chlorophyll data based on Moderate Resolution Imaging Spectroradiometer (MODIS)-AQUA and Visible and Infrared Imager/Radiometer Suite (VIIRS) having a spatial resolution of 4 km (Maritorena et al., 2010). Because of the frequent absence of chlorophyll data due to cloud cover, we use monthly averaged chlorophyll data at the mooring locations. Approximate values of V_1, V_2, ζ_1, and ζ_2 at the buoy location during the study period are 0.38, 0.62, 1.5 m, and 17 m, respectively.

Optimal interpolated (OI) Microwave and Infrared SST data at 9 km resolution (Gentemann et al., 2004) averaged over 50 km on either side of the buoy locations were used to estimate the horizontal gradients of SST in equation (1). The zonal (u) and meridional (v) components of velocity at 10 m depth were obtained from the RAMA buoys. From 2017 onward, Nortek Aquadopp Doppler current meters were used for current measurements at the 12°N and 8°N RAMA moorings. Otherwise, SonTek Argonaut Doppler current meters were used for current measurements at all RAMA mooring locations in the BoB. Moreover, we considered only those time periods when all the in situ data were available from the mooring so that all terms could be computed contemporaneously. This condition was met approximately 29%, 48%, and 52% of the time at 8°N, 12°N, and 15°N, respectively.

The residual in 1 includes neglected terms like horizontal and vertical diffusive heat fluxes, plus instrumental, sampling, and computational errors involving all the other resolved terms. Earlier studies have shown that vertical diffusive heat fluxes below the ML are often the largest contributor to the residual term (Bond & McPhaden, 1995; Cronin et al., 2015). Thus, we will estimate this term by assuming that residual is all due primarily to vertical diffusive heat fluxes rather than to other unresolved processes or to errors (Bond & McPhaden, 1995; Cronin et al., 2015; McPhaden, 1982; Scannell & McPhaden, 2018; Wang & McPhaden, 1999).

In order to estimate the vertical heat diffusivity from the ML heat budget residual, we adopt filtering criteria from Cronin et al. (2015) with the assumption that these filtering criteria minimize the impact of errors in the residual, though for comparison we present the vertical heat diffusivity computed without any filtering criterion (Criterion 1). We start by assuming that diffusion results from downgradient heat fluxes and thus, as Criterion 2, consider only positive diffusivity. Specifically, we consider only downgradient heat flux to estimate the vertical heat diffusivity such that vertical heat diffusivity is computed from residual fluxes either positive within the presence of a positive temperature gradient at the base of ML or negative within the presence of a negative temperature gradient at the base of ML. We defined filtering Criterion 2 (downgradient) as the "base filtering" criterion, such that we examined the impact of all other filtering criterion/criteria in combination with Criterion 2.

As suggested by Cronin et al. (2015) in the presence of a small vertical temperature gradient, the residual may not be associated with vertical heat diffusivity. Hence, we introduce another filtering criterion (Criterion 3; strong gradient) such that diffusivity is calculated only when the temperature gradient is greater than 0.003 °C m^{-1} within 5 m below the MLD. As stated by Cronin et al. (2015), in the presence of strong currents, the residual term is dominated by heat flux due to the convergence of stratified shear flow. Hence, we prescribed two more filtering criteria such that the diffusivity is estimated only during periods when horizontal advection is less than two (Criterion 4; strong advection) and three (Criterion 5; very strong advection) standard deviations from its mean value.

A comparison between eddy heat fluxes estimated from temperature microstructure measurements on the RAMA mooring at 12°N, 90°E (Figure 6 of W16) and residual heat flux estimated based on ML temperature budget (supporting information Figure S1) indicates that the latter shows a large range with respect to the former. We assume that the large spread of values in the residual calculation indicates contamination by errors rather than eddy heat fluxes at the base of ML. Hence, we prescribed an additional filtering

Table 1
The Summary of Various Filtering Criteria Applied on Residual of ML Heat Budget to Estimate Vertical Heat Diffusivity

Criteria	Description [shorter form]
1	Without any filtering criterion
2	**Vertical heat diffusivity is computed from residual fluxes either positive within the presence of a positive temperature gradient at the base of ML or negative within the presence of a negative temperature gradient at the base of ML [downgradient].**
3	**Vertical heat diffusivity is calculated from residual fluxes only when the temperature gradient is greater than 0.003 °C m^{-1} within 5 m below the MLD [strong gradient].**
4	Vertical heat diffusivity is estimated from residual fluxes only during periods when horizontal advection is less than two standard deviations from its mean value [strong advection].
5	Vertical heat diffusivity is estimated from residual fluxes only during periods when horizontal advection is less than three standard deviations from its mean value [very strong advection].
6	Vertical heat diffusivity is computed from the residual fluxes when its magnitude was is less than two standard deviations from its mean [high residual].
7	Vertical heat diffusivity is computed from the residual fluxes when its magnitude was less than three standard deviations from its mean [very high residual].
8	**Vertical heat diffusivity is computed from the residual fluxes when either the BL is thinner than 15 m or the BL contains temperature inversions with magnitude greater than 0.2 °C [thick BL].**
9	Vertical heat diffusivity is computed from the residual fluxes when either the BL is thinner than 20 m or the BL contains temperature inversions with magnitude greater than 0.2 °C [very thick BL].

Note. The most important filtering criteria which we used in the present study are highlighted in the bold font. The shorthand names of each criterion are presented in the square brackets.

criterion to neglect the residual when its magnitude was greater than two (Criterion 6; high residual) or three (Criterion 7; very high residual) standard deviations from its mean.

The BL will inhibit mixing of heat below the ML. When the BL is thin (less than ~15 to 20 m), the MLD and ILD are close to one another, and the temperature gradient is largely negative at the base of the ML. In the case of a thick BL, the top of thermocline (equivalent to the base of the ILD) is far removed from ML and temperature is nearly uniform in the BL. This situation can result relatively small temperature gradients within the thick BL but also in some situations temperature inversions. Hence, we considered two more filtering criteria such that we only estimate the vertical heat diffusivity from the residual fluxes when the BL is either thinner than 15 m (Criterion 8) or 20 m (Criterion 9), or the BL contains a temperature inversion with magnitude greater than 0.2 °C.

For simplicity, the filtering criteria applied to estimate K_T are denoted with subscripts. The various filtering criteria described above are summarized in Table 1 along with their shorthand forms. For example, K_T estimated based on the filtering Criterion 2 and the combination of filtering Criteria 2, 3, and 8 are denoted as K_{T2} and K_{T238}, respectively. Following Cronin et al. (2015), 5 day smoothing is applied to the residual term before estimating vertical heat diffusivity to reduce random errors.

As mentioned earlier, the purpose of this study is to consider only downgradient heat fluxes and positive values of K_T. However, errors in K_T of both signs occur and can be large enough though to impact estimates of K_T. The variance of these errors is included in our estimates of K_{T1}, implying that estimates of K_{T1} are an upper bound on the variance of the vertical heat diffusivity. Similarly, after prescribing various filtering criteria, particularly after removing the upgradient fluxes from the residual (Criterion 2), seasonal medians and means of K_T represent an upper bound.

After prescribing these above mentioned filtering criteria, we categorized the data into four different seasons (spring: March–May; summer: June–September; fall: October–November; and winter: December–February). These seasons were chosen to correspond to the monsoon cycle. We also compare our results with W16 at 12°N during three periods: 1 December 2013 to 18 March 2014 (defined as w16_winter), the period 19 March 2014 to 5 May 2014 (defined as w16_spring), and the period 6 May 2014 to 24 September 2014 (defined as w16_summer). The 5 day smoothed residual heat fluxes during various seasons at the RAMA mooring locations before and after applying the various filtering criteria for the entire data record shows that there are a sufficient number of data points available to estimate seasonal medians of K_T (typically >150) except during fall for certain combinations of filtering criteria (Figure S1 and Tables S1 to S3).

The surface buoyancy flux is defined as the sum of a component due to surface heat flux ($\alpha Q_{net}/\rho C_p$) and a component due to freshwater flux ($\beta \rho S(P - E)$), where α is the coefficient of thermal expansion of seawater, C_p is heat capacity, Q_{net} is the net surface heat flux, β is the coefficient of haline contraction, P is the precipitation, and E is evaporation (Foltz , 2019). We calculate evaporation from latent heat flux using the expression $Q_{lat}/(\rho L_e)$, where L_e is the latent heat of vaporization, equal to $2.5 - (0.00236 \times \text{SST}) \times 10^6$ J kg^{-1} (Yu et al., 2008). The precipitation rate is estimated from TRMM 3B42 Version 7 data (Huffman et al., 2007).

The standard error of seasonal means and medians for each variable is estimated through bootstrap methods, which do not require the assumption of a normal distribution (Thomson & Emery, 2014).

3. Results

3.1. The Seasonal Cycle of Near-Surface Met-Ocean Parameter in the BoB

As background, we describe a few characteristics of the regional climatology in the BoB, including the seasonal evolution of SST, surface winds, total surface heat flux (Figure 1), and daily time series of near-surface oceanographic and meteorological parameters from the RAMA mooring at 12°N, 90°E for the period 2008–2018 (Figure 2). The near-surface wind field shows a strong annual cycle with prevailing circulation being northeasterly during winter and southwesterly during summer (Figures 1 and 2). The magnitude of wind speed is relatively high during summer and winter and low during spring and fall. Near-surface air is relatively moist during summer (relative humidity 85%) and dry during winter (relative humidity 65%). These differences are attributed to supply of moist air into the BoB by southwesterly winds during summer and the intrusion of dry continental air into the BoB by northeasterly winds during winter (Figures 1 and 2) (Prasad, 2004; Rao & Sivakumar, 2003; Thangaprakash et al., 2016). In general, the near-surface current structure does not show temporal coherence with respect to the seasonal evolution of the surface winds. Instead, it shows higher frequency fluctuations that are likely associated with prominent intraseasonal variability due to westward propagating Rossby Waves and eddies in the BoB (Figure 2) (Girishkumar, Ravichandran, & McPhaden, 2013).

SST and air temperature show strong semiannual cycles with warming during the spring and fall (March–April and October–November) and cooling during the summer and the winter (Figures 1 and 2). Surface salinity field shows minimum during February–May. Near-surface salinity is also low (31–33 psu) with respect to subsurface salinity (35 psu) which leads to a sharp halocline in the near-surface layer (Figure 2). The BL is relatively thick (~40 m) during November–February in association with a thin ML due to freshening near the surface, while during spring and summer, the BL and ML are thinner (Figure 2) (Girishkumar et al., 2011; Rao & Sivakumar, 2003; Thadathil et al., 2007).

Net shortwave radiation shows a strong seasonal cycle with maximum amplitude during spring (~290 W m^{-2}) and minimum during winter (~150 W m^{-2}) (Figure 2). Total surface heat flux (sum of net shortwave radiation, net longwave radiation, and latent and sensible heat flux) also shows a strong seasonal cycle with heat gain over most of the basin except during winter (Figure 1). Maximum heat gain occurs during spring (~80 W m^{-2}), while during summer and fall there is a heat gain of 20 to 40 and ~50 W m^{-2}, respectively (Figure 1). During winter, there is a −80 to −40 W m^{-2} total surface heat loss from the BoB (Figure 1).

3.2. Estimation of Vertical Heat Diffusivity at the Base of ML

Earlier studies have discussed the seasonal and intraseasonal variability of the ML heat budget using RAMA mooring data in the BoB (Girishkumar, Ravichandran, & McPhaden, 2013; Girishkumar et al., 2017; Thangaprakash et al., 2016; Thadathil et al., 2016). Our purpose here is to focus on the residuals of this heat budget and what they can tell us about diffusive heat flux at the base of ML. The temporal evolution of terms in the ML heat budget at the RAMA mooring locations (Figure 3) and its mean seasonal evolution based on annual and semiannual harmonics (Figure 4) shows that the net surface heat flux plays primary role the ML heat balance. For instance, the net surface heat flux at 15°N shows heat gain by the ocean during spring (65 W m^{-2}) and fall (30 W m^{-2}) and heat loss by the ocean during winter (−100 W m^{-2}) and peak of summer (−15 W m^{-2}) (Figure 4a).

It is also evident that entrainment below the ML (term d in equation 1) typically plays a secondary role (Figure 4a). At 15°N, entrainment shows a clear seasonal cycle with heating of the ML (20 W m^{-2}) during
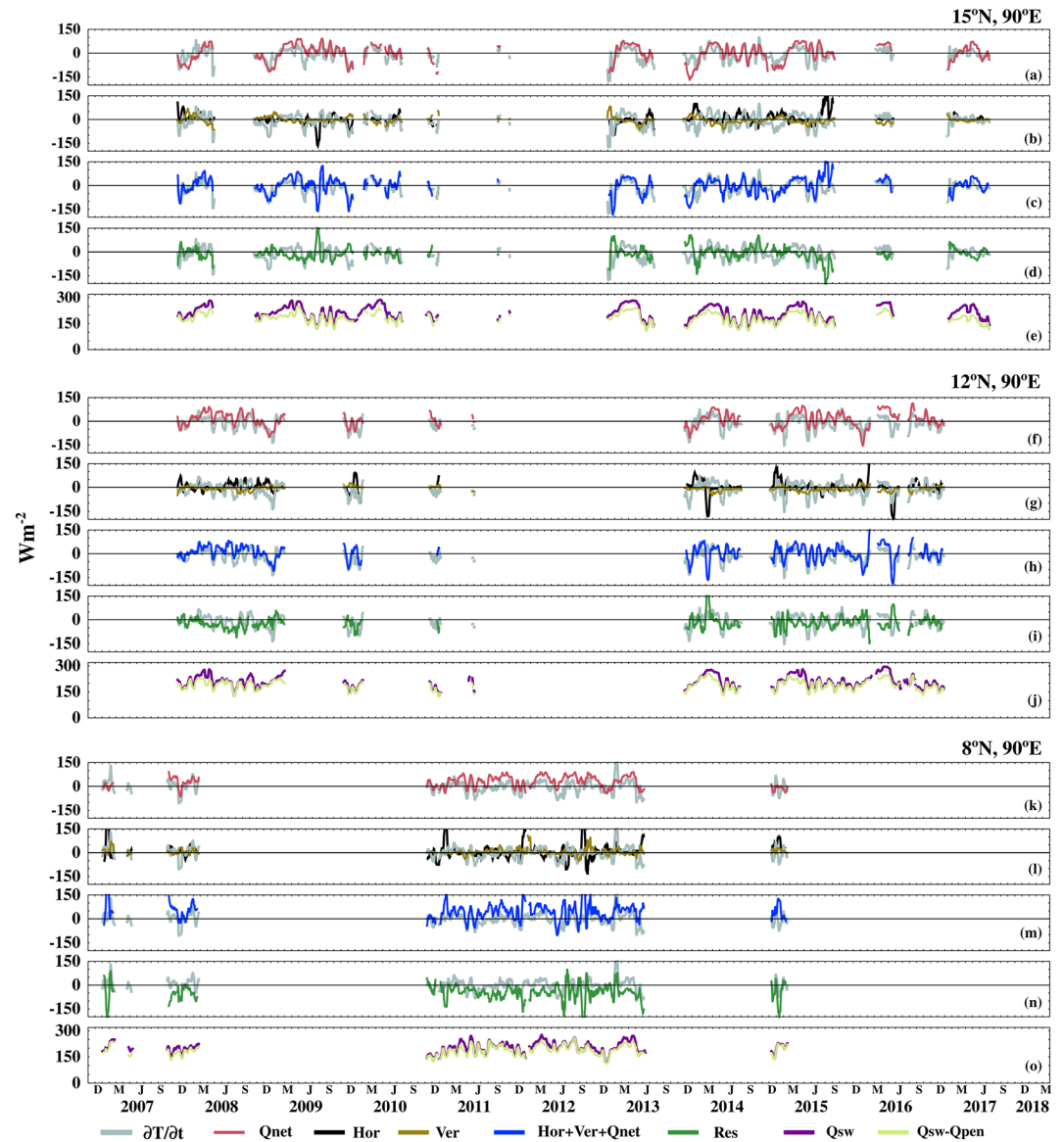
Figure 3. Terms in the ML heat budget (W m^{-2}) at 15°N, 90°E in the BoB. (a, f, and k) The ML heat storage rate (gray; $\partial T/\partial t$) and net surface heat flux (red; Q_{net}); (b, g, and l) the ML heat storage rate (gray; $\partial T/\partial t$), horizontal advection (black; Hor) and vertical heat flux (brown; Ver); (c, h, and m) the ML heat storage rate (gray; $\partial T/\partial t$), sum of net surface heat flux, horizontal advection, and vertical heat flux term (blue; Hor + Ver + Q_{net}); (d, i, and n) the ML heat storage rate (gray; $\partial T/\partial t$) and residual (green; Res); (e, j, and o) net shortwave radiation (purple; Q_{sw}) and net shortwave radiation − penetrative shortwave radiation below the ML (yellow; $Q_{sw} - Q_{pen}$). A 30 day running mean is applied to all data for a clear representation of lower frequency variations.

November–February and cooling (−25 W m^{-2}) during April–June (Figure 4a) (Prasad, 2004; Rao & Sivakumar, 2000; Shenoi et al., 2002; Thangaprakash et al., 2016). The positive tendency of the entrainment term during winter is physically realistic since it coincides with presence of strong and persistent occurrence of temperature inversions (Thangaprakash et al., 2016) (Figures 5 and 6). Similar tendencies with slightly difference in magnitude are observed at other mooring locations in the BoB (Figures 4a–4c).

In the following analysis we evaluate the impact of various filtering criteria (Criteria 2–9) on the estimation of K_T using the unfiltered K_T estimates (Criterion 1) as a baseline for the overlapping period of W16 (Table 2) and for the full time series (Tables S1–S3 and Figure 7). The analysis is based on base filtering Criterion 2 (downgradient only) plus a combination filtering Criteria 3 to 9 (i.e., K_{T2}, K_{T23}, K_{T24}, … and K_{T29}). In addition
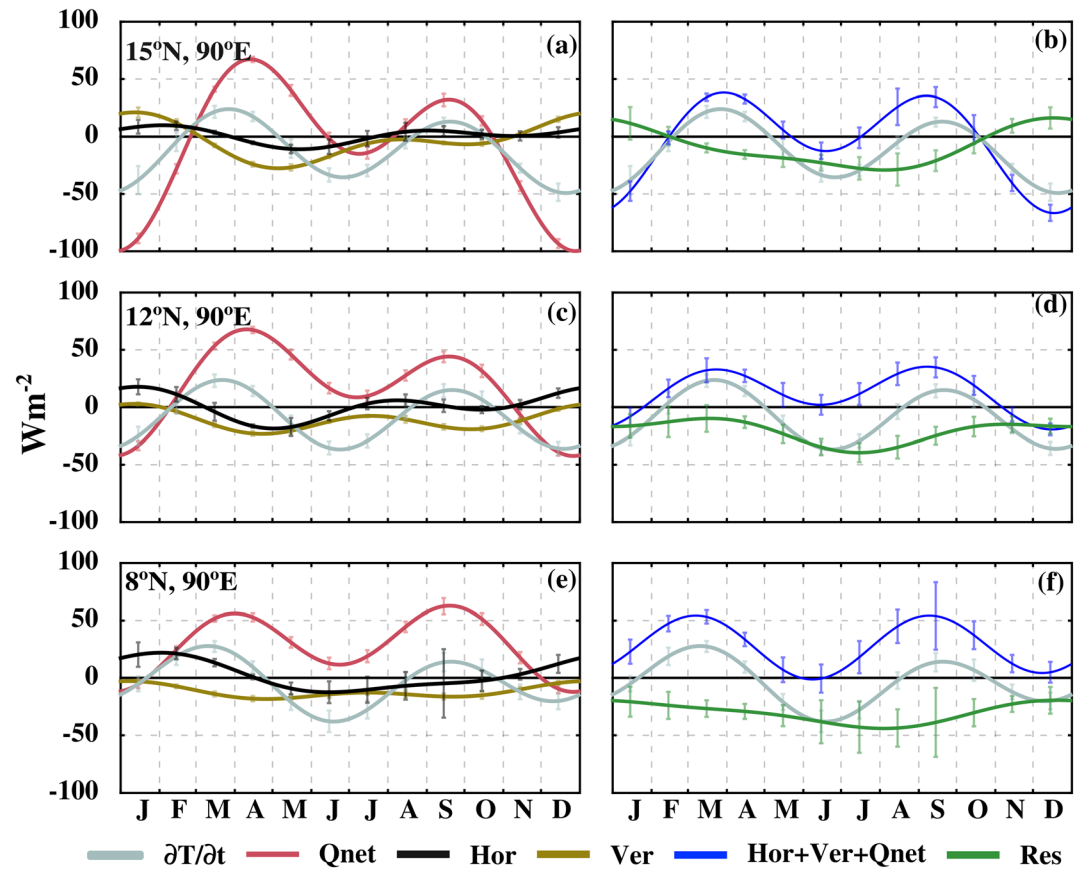
Figure 4. The seasonal evolution of terms in the ML heat budget in the mixed layer heat balance at (a and b) 15°N, 90°E (c and d) 12°N, 90°E, and (e and f) 8°N, 90°E RAMA mooring locations based on mean, annual, and semiannual harmonics. (a, c, and e) The ML heat storage rate (gray; $\partial T/\partial t$), net surface heat flux (red; Q_{net}), horizontal advection (black; Hor), and vertical heat process (brown; Ver). (b, d, and f) the ML heat storage rate (gray; $\partial T/\partial t$), sum of net surface heat flux, horizontal advection and vertical heat flux term (blue; Q_{net} + Hor + Ver), and residual (light green). The vertical bar represents one standard error using bootstrap methods for monthly means, estimated based on year-to-year deviations from the mean seasonal cycle. Units: W m^{-2}.

we also present the results based on combination of three or four filtering criteria such as K_{T238}, K_{T23578}, and K_{T23468}. The basic objective is to determine how much difference filtering criteria can make, which filtering criteria have the largest impact on the estimation of K_T, and how the different versions of K_T compare to the direct estimates of W16. The K_T estimates with no filtering criteria and after applying different filtering criteria to the residual of ML heat budget are presented in Tables 2 and S1–S3. Graphical representation of Tables S1–S3 is presented in Figure S2.

Bond and McPhaden (1995) showed that the difference between the estimation of vertical heat diffusivity from the residual of ML heat budget and direct vertical microstructure measurements is halved by considering the median instead of the mean residual. Moreover, W16 presented the median of daily average of eddy diffusivity instead of the mean. In this study we present both the seasonal median and mean of vertical heat diffusivity estimated from the residual of the ML heat budget and find that the variation of seasonal median K_T is relatively small compared to the variation of seasonal mean K_T with respect to various filtering criterion (Tables 2 and S1–S3 and Figure S2).

As stated earlier, errors in K_T of both signs before applying any filtering conditions are large enough to impact the estimates of eddy diffusivity of heat and may even lead to negative seasonal mean and median values of K_{T1} (Figure 7 and Table 2). For example, during w16_winter, the presence of a significant number of negative values of K_T leads to a negative seasonal mean ($-18.8 \times 10^{-4}\,\mathrm{m^2\,s^{-1}}$) before applying any filtering criterion (Table 2 and Figure 7).

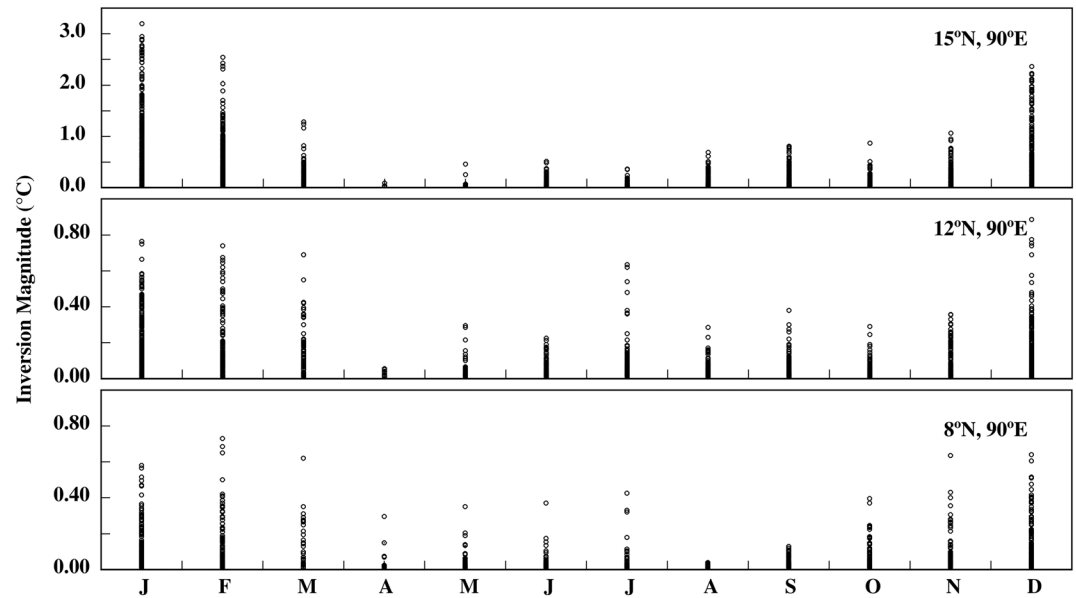**Figure 5.** The seasonal variability of magnitude of temperature inversion (°C) estimated from the daily averaged data at the RAMA mooring location in the BoB at (top) 15°N, 90°E; (middle) 12°N, 90°E; and (bottom) 8°N, 90°E. The y axis of the top panel is different from the other two panels.

With the addition of various filtering criteria to base filtering criterion, we find that the variation of seasonal median of K_T is relatively small compared to the variation of seasonal mean of K_T (Tables 2 and S1–S3 and Figure S2). For example, during w16_winter, the seasonal mean K_T varies over a factor of three magnitude (15.0×10^{-4} and 5.2×10^{-4} m^2 s^{-1}) while the variation of seasonal median of K_T is smaller (4.8×10^{-4} and 2.5×10^{-4} m^2 s^{-1}) over various filtering criteria (Criterion 2 to $2 + 3 + 8 + 6 + 4$) (Table 2). A plausible reason for this difference between estimates of the seasonal mean and median K_T is the skewed frequency distribution of K_T with a few very high values of K_T before applying filtering criteria along with the base filtering criterion ($2 =$ downgradient) (positive values in Figure 7a). In that situation, the median does not change
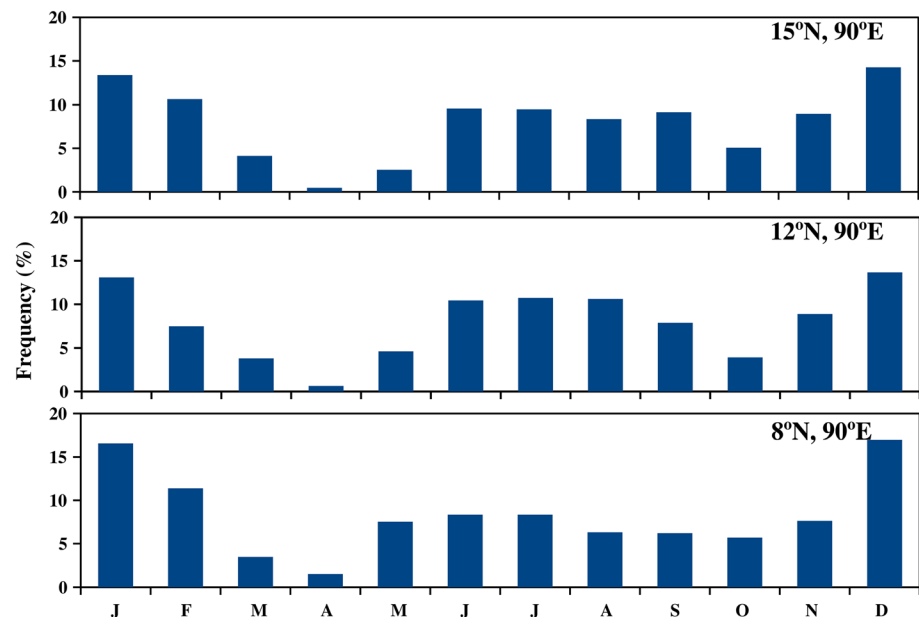

Figure 6. The seasonally varying frequency distribution (%) of temperature inversions (%) from the daily averaged data at the RAMA mooring location in the BoB at (top) 15°N, 90°E; (middle) 12°N, 90°E; and (bottom) 8°N, 90°E.

Table 2
Estimation of the Seasonal Median ± Standard Error and Mean ± One Standard Error of K_T ($m^2\,s^{-1}$) During the Similar Time Period of Warner et al. (2016) RAMA Mooring Location Based on 5 Day Smoothed Residual Heat Flux at 12°N and 90°E in the BoB

Warner period at 12°N	Winter (×10⁻⁴)			Spring (×10⁻⁴)			Summer (×10⁻⁴)		
	Median	Mean	ND	Median	Mean	ND	Median	Mean	ND
K_{T1} (Without filtering)	0.7 ± 0.5	-18.8 ± 9.6	103	0.1 ± 0.1	1.1 ± 0.9	48	1.7 ± 0.2	4.2 ± 1.5	86
K_{T2} (Res + ve with TI)	4.8 ± 1.3	15 ± 3	58	0.5 ± 0.2	3.5 ± 1.6	26	1.9 ± 0.2	4.9 ± 1.7	77
K_{T23} ($\partial T/\partial Z > 0.003\ °C\ m^{-1}$)	4.1 ± 1.1	11.1 ± 2.4	54	0.5 ± 0.2	3.5 ± 1.6	26	1.9 ± 0.2	2.8 ± 0.5	75
K_{T24} ($u\partial T/\partial x < 2$ STD)	4.1 ± 1.2	14.6 ± 3.2	54	0.5 ± 0.2	3.5 ± 1.6	26	1.9 ± 0.2	4.9 ± 1.7	77
K_{T25} ($u\partial T/\partial x < 3$ STD)	4.6 ± 1.2	14.7 ± 3.1	57	0.5 ± 0.2	3.5 ± 1.6	26	1.9 ± 0.2	4.9 ± 1.7	77
K_{T26} (Res < 2 STD)	4.8 ± 1.3	15 ± 3	58	0.5 ± 0.2	3.5 ± 1.6	26	1.9 ± 0.2	4.9 ± 1.7	77
K_{T27} (res < 3 STD)	4.8 ± 1.3	15 ± 3	58	0.5 ± 0.2	3.5 ± 1.6	26	1.9 ± 0.2	4.9 ± 1.7	77
K_{T28} (BLT < 15)	2.5 ± 0.7	5.9 ± 1.4	41	0.5 ± 0.2	0.7 ± 0.2	23	1.8 ± 0.2	3.8 ± 1.7	70
K_{T29} (BLT < 20)	3.5 ± 0.9	8.7 ± 1.8	48	0.5 ± 0.2	0.7 ± 0.2	23	1.9 ± 0.2	4.3 ± 1.7	75
K_{T238}	**2.5 ± 0.7**	**5.9 ± 1.4**	**41**	**0.5 ± 0.2**	**0.7 ± 0.2**	**23**	**1.8 ± 0.2**	**2.1 ± 0.3**	**69**
K_{T23578}	2.5 ± 0.7	5.9 ± 1.4	41	0.5 ± 0.2	0.7 ± 0.2	23	1.8 ± 0.2	2.1 ± 0.3	69
K_{T23468}	2.5 ± 0.6	5.2 ± 1.4	38	0.5 ± 0.2	0.7 ± 0.2	23	1.8 ± 0.2	2.1 ± 0.3	69
Without H									
K_{T1} (Without filtering)	1.5 ± 0.4	-13.3 ± 7.8	126	0.5 ± 0.2	2.2 ± 1.2	48	2.5 ± 0.2	5.2 ± 1.5	86
K_{T2} (Res + ve with TI)	4.4 ± 0.9	14 ± 2.5	79	0.7 ± 0.1	3.2 ± 1.4	39	2.7 ± 0.2	5.7 ± 1.6	81
K_{T238}	2.6 ± 0.7	6.1 ± 1.1	59	0.7 ± 0.1	0.8 ± 0.2	36	2.5 ± 0.2	2.9 ± 0.3	73
W16	**1.62**			**0.0085**			**2.39**		

Note. The seasons are defined based on Warner et al. (2016) (seasons: 1 December 2013 to 18 March 2014 as w16_winter, the period 19 March 2014 to 5 May 2014 as w16_spring, and the period 6 May 2014 to 24 September 2014 as w16_summer). The last row represents the seasonal median of K_T from W16. The K_{T238} values without detrainment are marked in bold font for better readability. ND = number of data points. If the difference between seasonal mean (median) of K_{T238} with and without detrainment is statistically significant at 99% confidence level based on t test (Mann-Whitney U test), these are marked in italics in the second last row (K_{T238}). In this table the difference in seasonal mean (median) of K_{T238} before and after incorporation of the detrainment process is not statistically significant at the 99% confidence level.

significantly, but the mean does with the elimination of high K_T values from the addition of various filtering criteria. For this reason, the median may be a more reliable estimate than the mean, which can be influenced by a few outliers in the probability distribution.

Our analysis further shows that the seasonal median and mean K_T converge after applying filtering Criteria 2 (downgradient), 3 (strong gradient), and 8 (thick BL). Note that incorporation of more filtering constraints to K_{T238} does not exclude a significant number of days. For example, K_{T23578} has the same number of days as K_{T238} in w16_winter (Table 2). Hence, incorporation of more filtering constraints does not have much impact relative to K_{T238}, such as ignoring the residual higher than two or three standard deviations and ignoring the residual value when horizontal advection is greater than two or three standard deviations, that is, K_{T23578} and K_{T23468} (Tables 2 and S1–S3). For instance, during w16_winter, the seasonal mean and median of K_T vary over a only a small range between K_{T238}, K_{T23578}, and K_{T23468} (5.9×10^{-4} to 5.2×10^{-4} m^2 s^{-1} for the mean and no change in the median; 2.5×10^{-4} m^2 s^{-1}) (Table 2). Hence, in the subsequent analysis we concentrate only on results for filtering Criteria 2 (downgradient), 3 (strong gradient), and 8 (thick BL).

In the ML heat budget, we considered only entrainment and ignored detrainment on the assumption that temperature is isothermal in the ML. In this situation, detrainment does not influence ML temperature. However, in practice the ML definition is based on a finite increment of stratification so that temperature may not be perfectly isothermal and a weak vertical temperature stratification can exist in the ML. Therefore, detrainment can have some effect in the ML heat budget, which we examine for W16 as in Cronin et al. (2015). Our analysis shows that for the majority of the cases, the difference in seasonal median and seasonal mean of K_{T238} before and after incorporation of the detrainment process is not statistically significant at the 99% confidence level (Tables 2 and S1–S3) based on a t test for seasonal means and the Mann-Whitney U test (a nonparametric test and does not require the assumption of normal distributions (Cardillo, 2009; Nachar, 2008) for seasonal medians. Henceforth, when we refer to the residual and K_T, we mean those values after applying filtering Criteria 2 (downgradient), 3 (strong gradient), and 8 (thick BL) without inclusion of detrainment unless otherwise noted.
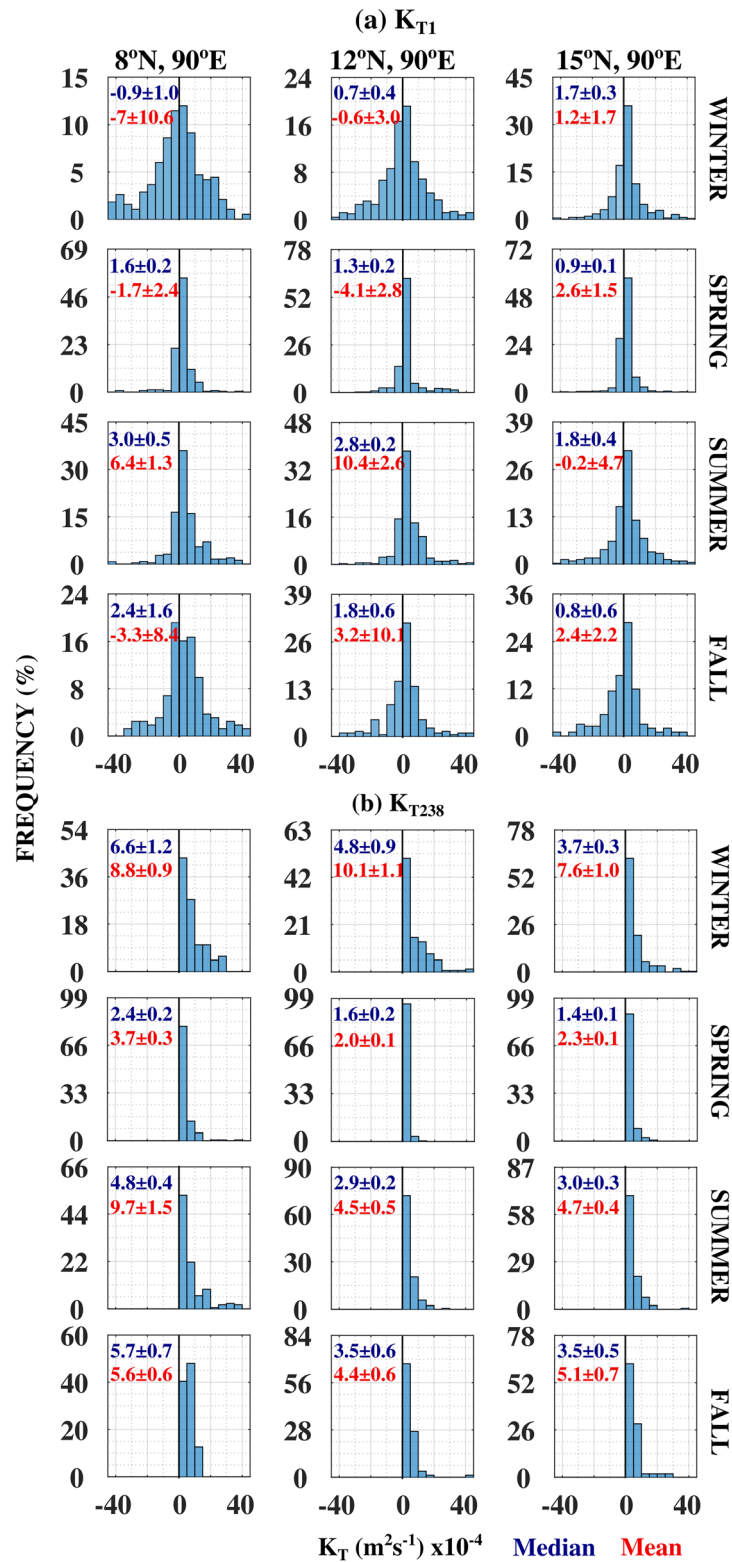
Figure 7. Frequency distribution (%) of K_T (m^2 s^{-1}) estimated from the residual of ML heat budget (a) before applying filtering criteria (K_{T1}) and (b) after applying filtering criteria (K_{T238}; 2 = downgradient, 3 = strong gradient, and 8 = thick barrier layer) at (left) 15°N, 90°E; (middle) 12°N, 90°E; and (right) 8°N, 90°E in the RAMA buoy location in the BoB during four different seasons spring (March–May), summer (June–September), fall (October–November), and winter (December–February). In panel (a) positive values represent vertical heat diffusivity values after applying base filtering criterion (K_{T2}; 2 = downgradient). The seasonal mean ± one standard error and seasonal median ± one standard error are indicated in blue and red in the respective panels.

At 12°N, the seasonal median of K_T estimated through residual of ML heat budget shows close agreement with W16 during the overlapping observation period (Table 2). During w16_winter, K_T estimated by W16 (1.6×10^{-4} m^2 s^{-1}) compares well with our analysis (2.5×10^{-4} m^2 s^{-1}) at 12°N, 90°E (Table 2). Similarly, during w16_summer, K_T estimated by W16 (2.4×10^{-4} m^2 s^{-1}) shows good agreement with our estimate (1.8×10^{-4} m^2 s^{-1}) (Table 2).

However, during w16_spring, our estimate of K_T (0.5×10^{-4} m^2 s^{-1}), which similar in magnitude to K_T in other seasons, is two orders of magnitude higher than the estimate of W16 based on microstructure measurements (8.5×10^{-7} m^2 s^{-1}). We speculate that this difference in estimates is primarily due to the MLD being shallower during spring in the BoB than the mooring temperature microstructure deployment depth (15 m) (Rao & Sivakumar, 2000; Sengupta et al., 2002). We estimate the percentage of time the MLD is shallower than 15 m during w16_spring at the 12°N RAMA mooring location and find that around 90% of time the MLD is shallower than 15 m. Thus, we argue that K_T as measured by W16 during the spring represents interior turbulence rather than elevated values in the ML and transition layer, leading to a significant underestimation in the vertical heat diffusivity. Indeed, the microstructure estimate of K_T during w16_spring is only 5 times larger than the molecular diffusivity of heat (1.5×10^{-7} m^2 s^{-1}) and a factor of 10 below typical thermocline values (2×10^{-6} to 7×10^{-6} m^2 s^{-1}) (Cherian et al., 2019; Sweers, 1970). Also, Thakur et al. (2019) found that vertical heat diffusivity near the base of the ML based on microstructure measurement at 18°N in the BoB was 1.5×10^{-5} m^2 s^{-1} during spring 2015, in good agreement with our estimate of K_T value during spring. This further supports our argument about the difference in the K_T estimated in this study and w16_spring being primarily associated with the position microstructure well below the shallow ML rather than at the base of the ML.

On the other hand, the majority of the time the MLD is deeper than 15 m during w16_winter (~90%) and w16_summer (~98%). This indicates that during w16_summer and w16_winter, the temperature microstructure at a fixed depth (15 m) is sometimes inside the ML, or below the ML or at the base of the ML. As reported by earlier studies using microstructure profiler data in different parts of the global ocean, diffusivities change rapidly from 10^{-2} m^2 s^{-1} in the upper part of the ML to 10^{-5} m^2 s^{-1} in the thermocline (Fernández-Castro et al., 2014; Hummels et al., 2013, 2014; Lozovatsky et al., 2006; Sun et al., 2013; Dohan & Davis, 2011). Hence, W16 estimates of seasonal eddy diffusivity of heat during w16_summer and w16_winter provide an average of values in and at the base of the ML.

We note that the order of magnitude of eddy diffusivity values at the base of ML reported in this study is similar to earlier studies in the tropical Atlantic (Hummels et al., 2014) and in the North Pacific (Cronin et al., 2015). Based on microstructure profiler data collected in the tropical Atlantic Hummels et al. (2014) found that the eddy diffusivity at the base of ML varies between 1.2×10^{-4} and 7×10^{-4} m^2 s^{-1}. In a similar type study as we performed here, Cronin et al. (2015) estimated eddy diffusivity values ranging from 1×10^{-4} to 6×10^{-4} m^2 s^{-1} in the North Pacific.

Hence, good correspondence between direct measurements of W16 and our indirect estimates during w16_summer and w16_winter indicates that the estimation of K_T from the residual of ML heat budget can be considered a reasonable upper bound of vertical heat diffusivity at the base of ML, consistent with Cronin et al. (2015) and Bond and McPhaden (1995). Thus, we extend the analysis to the RAMA mooring locations in the BoB at 8°N, 90°E; 12°N, 90°E; and 15°N, 90°E using all the available data (Figure 8 and Tables 3 and S1–S3). Values of K_{T238} estimated from the residual of ML heat budget during the entire data record indicates lower values during spring (1.4×10^{-4} to 2.4×10^{-4} m^2 s^{-1}) and higher values during winter (3.7×10^{-4} to 6.6×10^{-4} m^2 s^{-1}) compared to summer (2.9×10^{-4} to 4.8×10^{-4} m^2 s^{-1}) and fall (3.5×10^{-4} to 5.7×10^{-4} m^2 s^{-1}). In a particular season, the K_T values are relatively high at 8°N, 90°E compared to the other two mooring locations at 12°N, 90°E, and 15°N, 90°E (Table 3 and Figure 8). Since the number of 5 day smoothed residual heat flux data points available for the calculation of the K_T at the northern BoB during fall is relatively small (~40), these estimates should be viewed with caution.

We next examine the large-scale environmental factors that can influence the seasonal and latitudinal distribution of K_T at the three mooring sites. Surface buoyancy flux (B_0) and wind stress (τ) are the two important processes responsible for the generation of mixed layer turbulence (W16; Cronin & Sprintall, 2008; Fernández-Castro et al., 2014; Moum & Smyth, 2001; Moum et al., 2013; Thakur et al., 2019). Negative
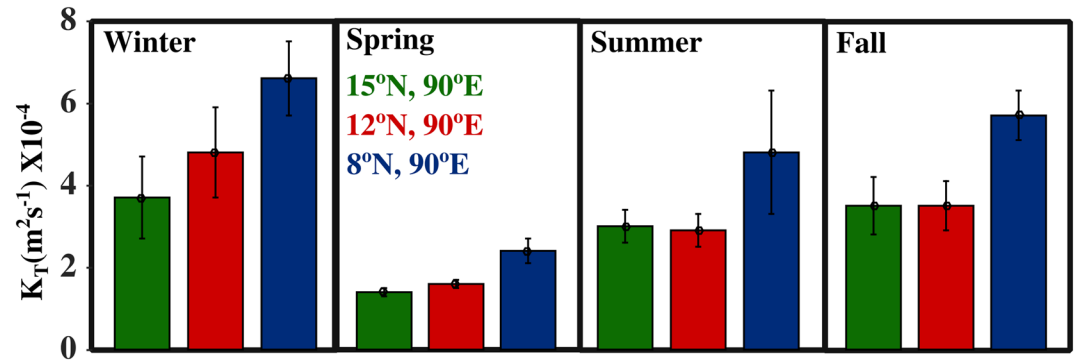
Figure 8. The seasonal median of K_T (m^2 s^{-1}) estimated from the residual of ML heat budget through filtering Criteria 2 (downgradient), 3 (strong gradient), and 8 (thick barrier layer) at three different mooring locations in the BoB at 15°N, 90°E (green); 12°N, 90°E (red); and 8°N, 90°E (blue) during winter, spring, summer, and fall. The error bar represents one standard error using bootstrap methods.

heat flux and higher evaporation over precipitation lead to negative buoyancy flux at the ocean surface causing the upper ocean to become unstable which in turn leads to turbulence generation. Conversely, positive heat flux and higher precipitation over evaporation leads to a stable upper ocean due to positive buoyancy flux (B_0) that favors turbulence suppression. Similarly, higher wind speed and lower stratification can enhance turbulence generation (W16; Cronin & Sprintall, 2008; Fernández-Castro et al., 2014; Moum & Smyth, 2001; Moum et al., 2013; Thakur et al., 2019). The seasonal average of wind stress (τ), buoyancy flux (B_0), Brunt-Vaisala frequency, $N^2 = -(g/\sigma_\theta)\,(\partial\sigma_\theta/\partial z)$, where σ_θ is the potential density at the base of ML (between ML and 5 m below the ML) and seasonal median of K_T estimated from the RAMA moorings in the BoB (Figure 9 and Table 4) show the relationship between spatial and seasonal variability atmospheric forcing and background stratification on K_T. We used B_0, τ, and N^2 values only when K_{T238} estimates were available to estimate its seasonal average.

During spring, wind stress is at its minimum (2.3×10^{-2} to 3.7×10^{-2} N m^{-2}), and buoyancy flux is maximum positive (8.0×10^{-6} to 8.7×10^{-6} kg s^{-1} m^{-2}) compared to other seasons in the BoB. Moreover, stratification is higher (~3.0×10^{-4} s^{-2}) at the base of ML without significant north to south variations. The combined effect of these atmospheric and oceanic conditions leads to a minimum K_T during spring (Figure 9 and Table 4). Southward enhancement of wind stress is consistent with the increasing tendency of K_T from north to south.

In contrast to spring, wind stress is higher (5.0×10^{-2} to 7.4×10^{-2} N m^{-2}) and buoyancy flux is negative (-5.2×10^6 to -3.1×10^6 kg s^{-1} m^{-2}) except at 8°N (2.2×10^6 kg s^{-1} m^{-2}) during winter. In addition, the stratification at the base of ML during winter (3.1×10^{-4} s^{-2} to 2.5×10^{-4} s^{-2}) is slightly lower than spring and summer (Figure 9 and Table 4) which in turn leads to maximum K_T values during winter. Southward enhancement of wind stress and reduction in stratification are plausible explanations for the southward enhancement of K_T during the winter (Table 4 and Figure 9).

Table 3
The Seasonal Median K_T (m^2 s^{-1}) ± One Standard Error After Applying Filtering Criteria 2, 3, and 8 on 5 Day Smoothed Residual Heat Flux at 8°N, 12°E, and 15°N in the RAMA Buoy Locations in the BoB During Four Different Seasons: Spring (March–May), Summer (June–September), Fall (October–November), and Winter (December–February)

Locations	Winter (×10^{-4}) DJF		Spring (×10^{-4}) MAM		Summer (×10^{-4}) JJAS		Fall (×10^{-4}) ON	
	Median ± SE	ND (in %)	Median ± SE	ND (in %)	Median ± SE	ND (in %)	Median ± SE	ND (in %)
15°N	3.7 ± 0.3	263 (50%)	1.4 ± 0.1	419 (62%)	3.0 ± 0.3	180 (36%)	3.5 ± 0.5	54 (27%)
12°N	4.8 ± 0.9	151 (29%)	1.6 ± 0.2	222 (61%)	2.9 ± 0.2	179 (49%)	3.5 ± 0.6	85 (40%)
8°N	6.6 ± 1.2	70 (18%)	2.4 ± 0.2	186 (67%)	4.8 ± 0.4	164 (64%)	5.7 ± 0.7	40 (23%)

Note. ND is the number of data points, and percentage of data points with respect to total points in respective seasons is indicated in the brackets. Note that the information in Table 3 is extracted from Tables S1–S3. The one standard error is estimated using bootstrap methods.
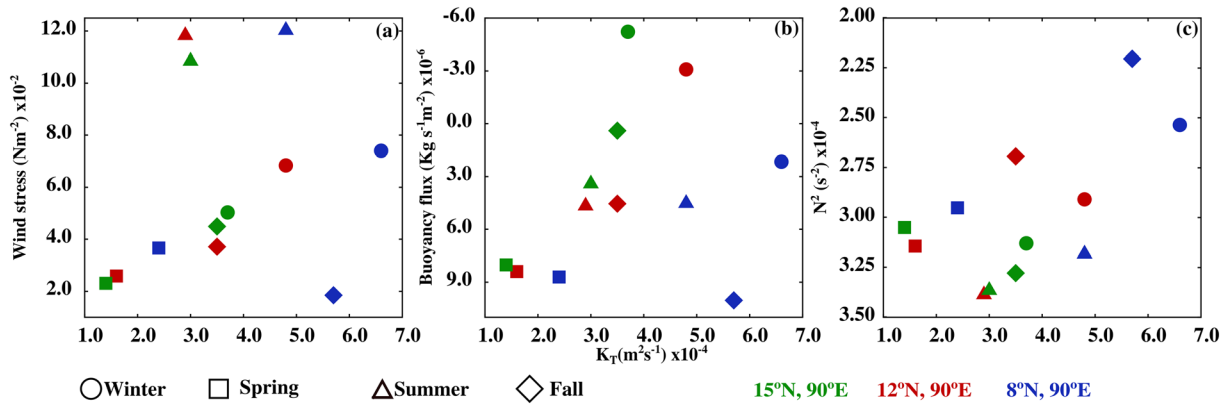
Figure 9. The seasonal (winter = circle; spring = square; summer = triangle and fall = diamond) median of K_{T238} estimated from the residual of ML heat budget against a wind stress ($\tau \times 10^{-2}$ N m^{-2}), (b) buoyancy flux ($B_0 \times 10^{-6}$; kg s^{-1} m^{-2}), and (c) Brunt-Vaisala frequency ($N^2 \times 10^{-4}$; s^{-2}), at different RAMA mooring locations in the BoB. Note that the y axis is reversed in panels (b) and (c).

During summer, K_T values are relatively small compared to winter, though the seasonal average wind stress (10.9×10^{-2} to 12.0×10^{-2} N m^{-2}) is higher. The presence of positive buoyancy flux (3.4×10^{-6} to 4.7×10^{-6} kg s^{-1} m^{-2}) and relatively higher stratification (3.2×10^{-4} to 3.4×10^{-4} s^{-2}) at the base of ML during summer compared to winter is a plausible explanation for this seasonal difference in K_T.

The above discussion provides a qualitative perspective on the relation between the three forcing factors (B_0, N^2, or τ) and their modulation of K_T. To quantify the relationship between the three forcing factors (B_0, N^2, or τ) on the seasonal variation of K_T in the BoB, we also performed simple linear and multiple linear regression analysis using combined data from the three sites (Figure 10) (Thomson & Emery, 2014). In the linear regression analysis with single independent variables (B_0, τ, or N^2), the magnitude of the regression coefficient (S) gives the strength of the association between independent variable(s) and dependent variable and the sign identifies whether there is a positive and negative relationship between dependent and independent variable K_T. The coefficient of determination (R^2) indicates the percentage of variance in the dependent variable explained by the independent variables. The p value of the t statistic (based on the regression coefficient divided by its standard error) provides the probability that the regression coefficient (S) is different from 0 (the null hypothesis).

Table 4
The Seasonal Mean $\pm$ One Standard Error of Buoyancy Flux ($B_0 \times 10^{-6}$; kg s^{-1} m^{-2}), Brunt-Vaisala frequency ($N^2 \times 10^{-4}$; s^{-2}), Wind Stress (τ; $\times 10^{-2}$ Nm^{-2}), and Seasonal Median of K_T Estimated From the Residual of ML Heat Budget at Different RAMA Mooring Location in the BoB

	B_0 ($\times 10^{-6}$) kg s^{-1} m^{-2}	N^2 ($\times 10^{-4}$) s^{-2}	τ ($\times 10^{-2}$) N m^{-2}	K_T ($\times 10^{-4}$) (m^2 s^{-1})
RAMA 15°N				
Winter	-5.2 ± 0.4	3.1 ± 0.1	5.0 ± 0.2	3.7 ± 1
Spring	8.0 ± 0.2	3.0 ± 0.1	2.3 ± 0.2	1.4 ± 0.1
Summer	3.4 ± 0.7	3.4 ± 0.2	10.9 ± 0.5	3.0 ± 0.4
Fall	0.4 ± 1.4	3.3 ± 0.3	4.5 ± 0.5	3.5 ± 0.7
RAMA 12°N				
Winter	-3.1 ± 0.8	2.9 ± 0.2	6.8 ± 0.3	4.8 ± 1.1
Spring	8.4 ± 0.4	3.1 ± 0.1	2.6 ± 0.3	1.6 ± 0.1
Summer	4.7 ± 0.6	3.4 ± 0.2	11.8 ± 0.5	2.9 ± 0.4
Fall	4.5 ± 0.6	2.7 ± 0.1	3.7 ± 0.3	3.5 ± 0.6
RAMA 8°N				
Winter	2.2 ± 1.4	2.5 ± 0.2	7.4 ± 0.7	6.6 ± 0.9
Spring	8.7 ± 1.4	3.0 ± 0.1	3.7 ± 0.4	2.4 ± 0.3
Summer	4.5 ± 0.5	3.2 ± 0.1	12.0 ± 0.4	4.8 ± 1.5
Fall	10.0 ± 1.1	2.2 ± 0.2	1.9 ± 0.4	5.7 ± 0.6

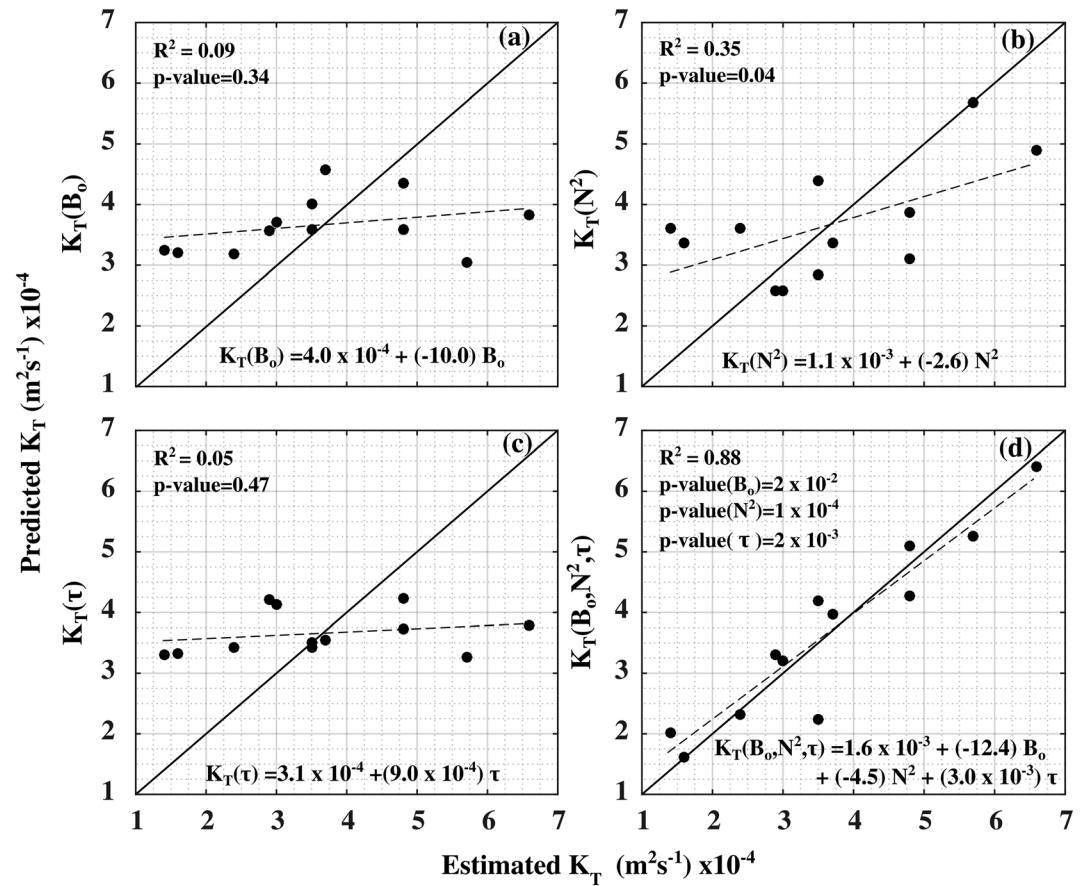*Note.* The error bar represents one standard error using bootstrap methods.

Figure 10. The scatter diagram between estimated K_{T238} and predicted K_{T238} based on single regression analysis between (a) B_0 and K_{T238}, (b) N^2 and K_{T238}, and (c) τ and K_{T238}, and (d) based on multiple regression analysis between hree independent forcing factors (B_0, τ, and N_2) and K_{T238}. In the panel R^2 represents the regression coefficient. The p value of the t statistic (based on the regression coefficient divided by its standard error) indicates the probability that the regression coefficient (S) is different from 0 (the null hypothesis). The regression equation is indicated in each panel. The black 1:1 line indicates perfect agreement. The dashed line represents the regression fit between estimated and predicted K_T.

The R^2 for the simple linear regression between independent variables (B_0, τ, or N^2) on to the dependent variable (K_T) are 0.09, 0.05, and 0.35 for B_0, τ, and N^2, respectively (Figure 10). The p value of the simple linear regression coefficient between N^2 and K_T is 0.04; hence, it is significant at the 95% confidence level. However, the simple linear regression coefficient between B_0 and K_T (τ and K_T) is significant at a 66% (53%) confidence level only. This indicates that N^2 is both significant and more influential than either B_0 and τ in modulating K_T.

However, for the multiple linear regression analysis between three independent forcing factors (B_0, τ, or N^2) and K_T, the R^2 increased to 0.88. The p values of the multiple regression coefficients are less than 0.05 for all independent variables, and hence they are significant at 95% confidence level. The relatively large change in R^2 value in the multiple regression compared to single regression between three forcing factors (B_0, τ, or N^2) and K_T implies that adding these three forcing factors together increases the K_T predictability on seasonal time scales in the BoB. This indicates that these forcing factors are more effective in combination than individually in explaining the seasonal variability of K_T. Moreover, the enhancement of R^2 in the multiple regression compared to the single regression implies that there is a dependency between the forcing factors. For instance, positive buoyancy flux (B_0) leads to an enhancement of upper-ocean stratification (N^2). We find that K_T predicted by multiple regression compares best with the estimated K_T (Figure 10). This analysis
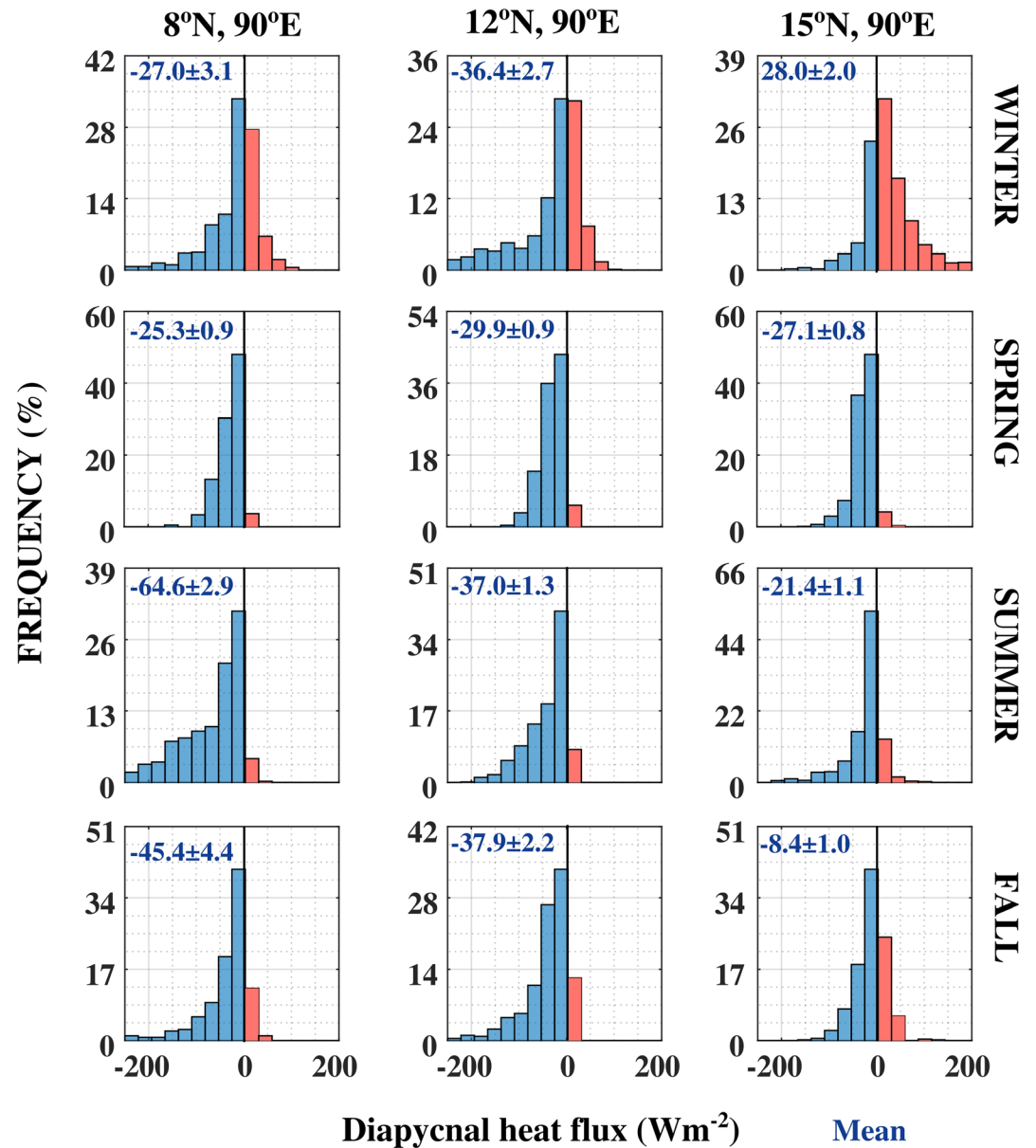
Figure 11. Frequency distribution (%) of vertical diffusive heat flux (W m^{-2}) estimated based on K_{T238} at (left) 15°N, 90°E; (middle) 12°N, 90°E; and (right) 8°N, 90°E in the BoB during four different seasons spring (March–May), summer (June–September), fall (October–November), and winter (December–February). Positive and negative values are represented in the red and blue, respectively. The seasonal mean ± one standard error is indicated in blue in the respective panels.

demonstrates that B_0, τ, and N^2 together determine the seasonal modulation of K_T, though as with the simple linear regression results, N^2 is the most significant determinant.

3.3. Estimation of Vertical Diffusive Heat Flux at the Base of ML

Based on the seasonal median of vertical heat diffusivity of heat (K_{T238}) and the time-varying temperature gradient at the base of ML ($\partial T / \partial Z$) over the full record length for which we can compute ($\partial T / \partial Z$), we estimate the vertical diffusive heat flux at the base of ML at the three mooring locations in the BoB. In general, the frequency distribution of the vertical diffusive heat flux peaks between −25 to −50 W m^{-2} with a long tail towards large negative values in some seasons (Figure 11). For example, during summer in the southern BoB (8°N), the frequency distribution shows significant number of high negative values between −150 and

Table 5

Seasonal Mean ± One Standard Error of Vertical Diffusive Heat Flux (W m^{-2}) at the Base of ML Based on the Seasonal Median of K_{T238} at 8°N, 12°E, and 15°N in the RAMA Buoy Locations in the BoB During Four Different Seasons: Spring (March–May), Summer (June–September), Fall (October–November), and Winter (December–February)

	Winter	Spring	Summer	Fall
15°N, 90°E	28.0 ± 2.0	−27.1 ± 0.8	−21.4 ± 1.1	−8.4 ± 1.0
12°N, 90°E	−36.4 ± 2.7	−29.9 ± 0.9	−37.0 ± 1.3	−37.9 ± 2.2
8°N, 90°E	−27.0 ± 3.1	−25.3 ± 0.9	−64.6 ± 2.9	−45.4 ± 4.4

Note. The error bar represents one standard error using bootstrap methods.

200 W m^{-2}, and it must be associated with moderately high vertical heat diffusivity and presence of strong temperature gradient at the base of ML. Due to the presence of persistent temperature inversions, the vertical diffusive heat flux shows significant positive heat flux values during winter, particularly in the northern BoB (Figure 11). A similar frequency distribution was observed for vertical diffusive heat flux estimated by W16 (cf. Figure 6 of W16 and Figure 11).

The seasonal average of vertical diffusive heat flux at the base of ML during summer shows larger negative values to the south (−64 W m^{-2}) than to the north (−21 W m^{-2}) (Table 5 and Figure 12). During winter, vertical diffusive heat flux shows a positive tendency (28 W m^{-2}) at 15°N and cooling tendency with comparable magnitude at 8°N and 12°N (~ −36 to −27 W m^{-2}) (Table 5 and Figure 12). The strong warming tendency during winter at 15°N is attributed to the persistent occurrence of strong temperature inversions, which are less frequent, relatively weak, and transient in nature in the southern BoB (Rao & Sivakumar, 2000; Thadathil et al., 2016; Thangaprakash et al., 2016) (Figures 5 and 6). In fall, the vertical diffusive heat flux is minimum in the northern BoB (−8 W m^{-2}) compared to south (~ −38 to −45 W m^{-2}). The low value of vertical diffusive heat flux in the north maybe associated with the presence of strong temperature inversions in the northern BoB, which can counterbalance negative values in the seasonal average. During spring, the vertical diffusive heat flux is approximately −30 to −25 W m^{-2} without any significant north south gradient.

The study by Hummels et al. (2014) shows that incorporation of vertical diffusive heat flux improves the ML heat budget in the equatorial Atlantic. To understand to what extent vertical diffusive heat flux term reduces the imbalance in the BoB ML heat budget, we examined the difference in the statistics before and after incorporation of the vertical diffusive heat flux term (Figure 13) using the seasonal median of K_T and time-varying thermal stratification. Adding the diffusive heat flux term in this way reduced the Root Mean Square Difference (RMSD) between the ML heat storage rate and the sum of contributing terms from 18.1 to 16.2 W m^{-2} (15°N), 23.3 to 11.1 W m^{-2} (12°N), and 33.1 to 28.2 W m^{-2} (8°N). Improvement was best at 12°N, but small at the other two locations and not uniform throughout the seasons. For example, at 15°N, addition of the diffusion term increased the imbalance in the ML heat budget during winter. This discrepancy may arise from using the seasonal median of K_T instead of time-varying K_T to estimate vertical
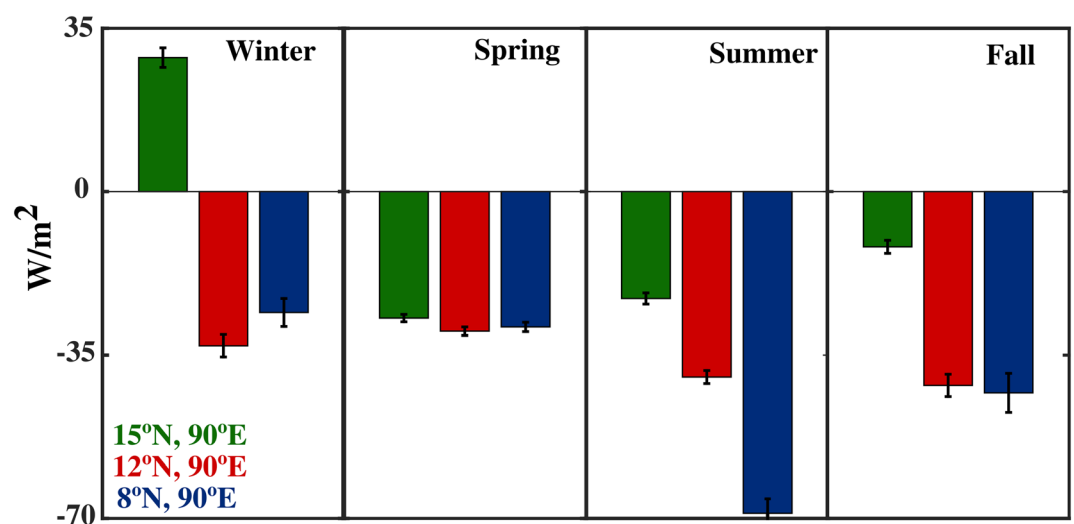

Figure 12. Seasonal average of vertical diffusive heat flux (W m^{-2}) at the base of ML based on seasonal median of K_{T238} and time-varying temperature gradient ($\partial T/\partial Z$; when K_{T1} values are available) at the base of ML at 8°N (blue), 12°E (red), and 15°N (green) in the RAMA buoy locations along 90°E in the BoB during four different seasons spring (March–May), summer (June–September), fall (October–November), and winter (December–February). The error bar represents one standard error using bootstrap methods.
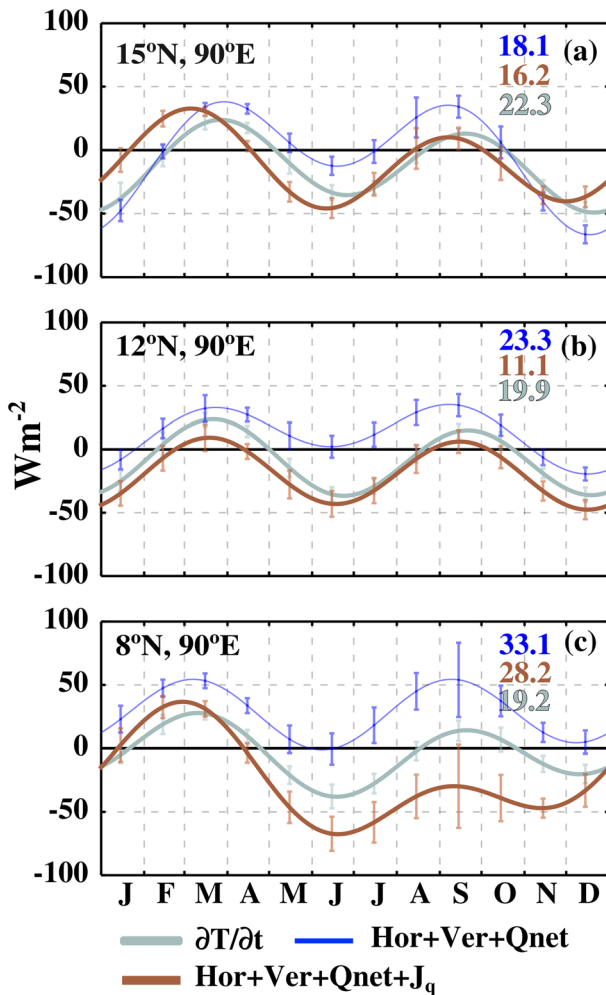
Figure 13. The seasonal evolution of the mixed layer heat balance before and after incorporation of vertical diffusive heat flux term in the sum of contributing terms at (a) 15°N, 90°E; (b) 12°N, 90°E; and (c) 8°N, 90°E RAMA mooring locations based on mean, annual, and semiannual harmonics. The ML heat storage rate (gray; $\partial T/\partial t$); sum of net surface heat flux, horizontal advection, and vertical heat flux term (blue; Q_{net} + Hor + Ver); and sum of net surface heat flux, horizontal advection, vertical heat flux term, and vertical diffusive heat flux (brown; Q_{net} + Hor + Ver + J_q). The vertical bars in gray, blue, and brown represent one standard error using bootstrap methods for ML heat storage rate and the sum of contributing terms with and without detrainment, respectively, and it is estimated based on year-to-year deviations from the mean seasonal cycle. The blue and brown numbers represent RMSD between ML heat storage rate and the sum of contributing terms with and without detrainment, respectively. Gray numbers represent the standard deviation of ML heat storage rate. Units: W m^{-2}.

diffusive heat flux. As demonstrated by W16 and Thakur et al. (2019) K_T has significant subseasonal variations in response to surface forcing and stratification. Nevertheless, the above analysis highlights the importance of accurately representing diffusive heat fluxes at the base on ML to determine the seasonal evolution of SST.

4. Summary and Discussion

Eddy diffusivity of heat (K_T) can be estimated through direct measurements of microstructure temperature. However, microstructure measurements are limited in space and time, so several studies have made an alternative attempt to estimate the eddy heat diffusivity through the residual of ML heat budget. We performed such calculations in the BoB using a refined methodology based on selecting periods when conditions were optimal for estimating the diffusivity following Cronin et al. (2015). For this purpose, we used moored buoy time series data at 15°N, 12°N, and 8°N along 90°E to estimate the seasonal average of vertical heat diffusivity and the heat flux at the base of ML in the BoB.

Following Cronin et al. (2015), we considered eight filtering criteria and separately and in combination. We evaluated how much difference filtering criteria can make and which filtering procedure had the largest impact on the estimation of K_T. We also compared our estimates with direct turbulent measurements in W16. Our analysis shows that at 12°N, the seasonal median K_T estimated through combination of filtering Criteria 2 (downgradient), 3 (strong gradient), and 8 (thick BL) shows generally close agreement with respect to Warner et al. (2016; W16) during similar observation periods in which the microstructure sensors sampled the ML. Given this good agreement with W16, we extended the analysis to all the RAMA mooring locations in the BoB using all the available data.

The present study illustrates the seasonal and spatial variability of K_T at the base of ML in the BoB. The K_T estimated from the residual of the ML heat budget during the entire data record indicates lower values during spring (1.4×10^{-4} to 2.4×10^{-4} m^2 s^{-1}) and higher values during winter (3.7×10^{-4} to 6.6×10^{-4} m^2 s^{-1}) compared to summer (2.9×10^{-4} to 4.8×10^{-4} m^2 s^{-1}) and fall (3.5×10^{-4} to 5.7×10^{-4} m^2 s^{-1}) at the mooring locations. Moreover, our analysis shows that in a particular season, the K_T values are relatively high at the southern BoB location (8°N, 90°E) compared to northern BoB sites (12°N, 90°E and 15°N, 90°E). The present study also shows that the presence of seasonal and spatial variability of K_T at the base of ML is modulated by stratification (N^2) at the base of ML and seasonal and spatial heterogeneity in atmospheric forcing such as wind stress (τ) and buoyancy flux (B_0). Simple linear and multiple regression analyses between the three atmospheric forcing parameters (B_0, N^2, or τ) and K_T demonstrate that B_0, τ, and N^2 together determine the seasonal modulation of K_T, though N^2 act as the primary determining factor.

The mooring data used for estimate the K_T covers differing periods, particularly at 12°N and 8°N (Figure 3). It is well known that near-surface atmospheric forcing and stratification in the BoB exhibit significant interannual variability (Girishkumar, Ravichandran & McPaden 2013; Pant et al., 2015), so that regional contrasts in seasonal diffusivity between three sites as described in this study may partially be affected by this interannual variability. However, we note that for the particular period of our study, interannual variability was weak so that our results more likely reflect spatial rather than year-to-year variations in K_T.

Based on these seasonal medians of vertical heat diffusivity, seasonal averages of vertical diffusive heat flux at the base of ML were estimated at the mooring locations in the BoB. The seasonal average of vertical diffusive heat flux at the base of ML shows strong latitudinal variation during fall (−8.4 to −45 W m^{-2}) and summer (−21 to −64 W m^{-2}) with maximum magnitude in the south and minimum at north. During winter, due to the persistent occurrence of strong temperature inversions in the north compared to the south, vertical diffusive heat flux shows a warming tendency (28 W m^{-2}) at 15°N but a cooling tendency at 8°N and 12°N (−36 to −27 W m^{-2}). The influence of temperature inversions was also observed during fall, with a minimum cooling tendency in the north (−8 W m^{-2}) compared to the south (−45 W m^{-2}). During spring, the vertical diffusive heat flux shows comparable in magnitude (~ −30 to −25 W m^{-2}) at all the RAMA mooring location in the BoB.

Our analysis shows that the incorporation of vertical diffusive heat fluxes in the ML heat budget equation reduces the imbalance in the ML heat budget. In particular, with diffusive heat flux included, the RMSD between the ML heat storage rate and the sum of contributing terms was reduced from 18.1 to 16.2 W m^{-2} at 15°N, from 23.3 to 11.1 W m^{-2} at 12°N, and from 33.1 to 28.2 W m^{-2} at 8°N. At 12°N, moreover, the imbalance was reduced significantly for all seasons.

Previous studies have shown that in the northern Indian Ocean, the oceanic component of coupled models used for seasonal and subseasonal forecasting and for future climate change projections shows a systematic SST error that leads to significant bias in the model simulations of monsoon precipitation (Levine et al., 2013; Pokhrel et al., 2012; Seo et al., 2009; Yu et al., 2012). Thus, in order to properly represent air-sea interaction processes, it is important accurately simulates SST in models. The source of the SST bias maybe associated with inappropriate representation of surface heat fluxes, wind stress, and/or vertical diffusive heat fluxes at the base of ML. Climate models parameterize vertical diffusive heat flux at the base of ML through the vertical temperature gradient and eddy diffusivity (K_T) Large et al. (1994). However, one of the key uncertainties in ocean models is lack of knowledge of the spatial and seasonal heterogeneity of K_T which is difficult to estimate directly via in situ measurements. In this study we adopted an alternative approach to estimate the upper bound on K_T from the residual of the ML heat budget consistent earlier studies (Bond & McPhaden, 1995; Cronin et al., 2015). Our definition of spatial and seasonal variability in K_T should facilitate the evaluation of turbulent mixing parameterization schemes incorporated in ocean models and help to quantify the source of model SST bias in coupled models. The maintenance of RAMA mooring network in the BoB for more than a decade has enabled us to perform the analysis. Very recently, RAMA was extended to the Arabian Sea where it will provide an opportunity to carry out a similar analysis with newly available observations there.

References

Bond, N. A., & McPhaden, M. J. (1995). An indirect estimate of the diurnal cycle in upper ocean turbulent heat fluxes at the equator, 140°W. *Journal of Geophysical Research*, *100*, 18 369–18 378.

Cardillo G. (2009). MWWTEST: Mann-Whitney-Wilcoxon non parametric test for two unpaired samples. http://www.mathworks.com/matlabcentral/fileexchange/25830.

Cherian, D. A., Shroyer, E. L., Wijesekera, H. W., & Moum, J. N. (2019). The seasonal cycle of upper-ocean mixing at 8°N in the Bay of Bengal. *Journal of Physical Oceanography*, *50*, 323–342>. https://doi.org/10.1175/JPO-D-19-0114.1

Cronin, M. F. & Sprintall, J. (2008). Wind and buoyancy-forced upper ocean. In J. H. Steele, (Eds.), *Encyclopedia of ocean sciences* (Vol. 6, pp. 337–345). Oxford, UK, ISBN 0–12–227430-x: Elsevier. https://doi.org/10.1016/B978-012374473-9.00624-X

Cronin, M. F., Pelland, N. A., Emerson, S. R., & Crawford, W. R. (2015). Estimating diffusivity from the mixed layer heat and salt balances in the North Pacific. *Journal of Geophysical Research: Oceans*, *120*, 7346–7362. https://doi.org/10.1002/2015JC011010

de Boisseson, E., Thierry, V., Mercier, H., & Caniaux, G. (2010). Mixed layer heat budget in the Iceland Basin from Argo. *Journal of Geophysical Research*, *115*, C10055. https://doi.org/10.1029/2010JC006283

Dickey, T. D., Manov, D. V., Weller, R. A., & Siegel, D. A. (1994). Determination of longwave heat flux at the air-sea interface using measurements from buoy platforms. *Journal of Atmospheric and Oceanic Technology*, *11*(4), 1,057–1,078. https://doi.org/10.1175/1520-0426(1994)0112.0.CO;2

Dohan, K., & Davis, R. E. (2011). Mixing in the transition layer during two storm events. *Journal of Physical Oceanography*, *41*, 42–66. https://doi.org/10.1175/2010JPO4253.1

Fairall, C. W., Bradley, E. F., Hare, J. E., Grachev, A. A., & Edson, J. B. (2003). Bulk parameterization of air-sea fluxes: Updates and verification for the COARE algorithm. *Journal of Climate*, *16*, 571–591. https://doi.org/10.1175/1520-0442(2003)016<0571:BPOASF>2.0.CO;2

Fernández-Castro, B., Mouriño-Carballido, B., Benítez-Barrios, V. M., Chouciño, P., Fraile-Nuez, E., Graña, R., et al. (2014). Microstructure turbulence and diffusivity parameterization in the tropical and subtropical Atlantic, Pacific and Indian Oceans during the Malaspina 2010 expedition. *Deep Sea Research, Part I*, *94*, 15–30.

Foltz, G. R. (2019). Wind- and buoyancy-forced upper ocean. In J. K. Cochran, J. H. Bokuniewicz, & L. P. Yager (Eds.), *Encyclopedia of ocean sciences* (3rd ed., Vol. 1, pp. 113–121)., Oxford: Elsevier. ISBN: 978-0-12-813081-0.

Foltz, G. R., & McPhaden, M. J. (2005). Mixed layer heat balance on intraseasonal time scales in the northwestern tropical Atlantic Ocean. *Journal of Climate*, *18*, 4168–4184. https://doi.org/10.1175/JCLI3531.1

Foltz, G. R., Vialard, J., Kumar, B. P., & McPhaden, M. J. (2010). Seasonal mixed layer heat balance of the southwestern tropical Indian Ocean. *Journal of Physical Oceanography*, *40*, 947–965.

Gentemann, C. L., Wick, G. A., Cummings, J., & Bayler, E. (2004). Multi-sensor improved sea surface temperature (MISST) for GODAE, presented at 13th Conference on Satellite Meteorology and Oceanography, Norfolk, VA, USA, 19-23, September, 2004. (http://www.remss.com/papers/gentemann/gentemann_13satmet_2004.pdf).

Girishkumar, M. S., Joseph, J., Thangaprakash, V. P., Pottapinjara, V., & McPhaden, M. J. (2017). Mixed layer temperature budget for the northward propagating Summer Monsoon Intraseasonal Oscillation (MISO) in the Central Bay of Bengal. *Journal of Geophysical Research: Oceans*, *122*, 8841–8854. https://doi.org/10.1002/2017JC013073

Girishkumar, M. S., Ravichandran, M., & Han, W. (2013). Observed intraseasonal thermocline variability in the Bay of Bengal. *Journal of Geophysical Research: Oceans*, *118*, 3336–3349. https://doi.org/10.1002/jgrc.20245

Girishkumar, M. S., Ravichandran, M., & McPhaden, M. J. (2013). Temperature inversions and their influence on the mixed layer heat budget during the winters of 2006–2007 and 2007–2008 in the Bay of Bengal. *Journal of Geophysical Research: Oceans*, *118*, 2426–2437. https://doi.org/10.1002/jgrc.20192

Girishkumar, M. S., Ravichandran, M., McPhaden, M. J., & Rao, R. R. (2011). Intraseasonal variability in barrier layer thickness in the south central BoB. *Journal of Geophysical Research*, *116*, C03009. https://doi.org/10.1029/2010JC006657

Huffman, G. J., Bolvin, D. T., Nelkin, E. J., Wolff, D. B., Adler, R. F., Gu, G., et al. (2007). The TRMM multi-satellite precipitation analysis: Quasi-global, multi-year, combined-sensor precipitation estimates at fine scale. *Journal of Hydrometeorology*, *8*(1), 38–55.

Hummels, R., Dengler, M., & Bourles, B. (2013). Seasonal and regional variability of upper ocean diapycnal heat flux in the Atlantic cold tongue. *Progress in Oceanography*, *111*, 52–74. https://doi.org/10.1016/j.pocean.2012.11.001

Hummels, R., Dengler, M., Brandt, P., & Schlundt, M. (2014). Diapycnal heat flux and mixed layer heat budget within the Atlantic cold tongue. *Climate Dynamics*, *43*(11), 3179–3199. https://doi.org/10.1007/s00382-014-2339-6

Kolodziejczyk, N., & Gaillard, F. (2013). Variability of the heat and salt budget in the subtropical southeastern Pacific mixed layer between 2004 and 2010: Spice injection mechanism. *Journal of Physical Oceanography*, *43*, 1880–1898. https://doi.org/10.1175/JPO-D-13-04.1

Large, W., McWilliams, J., & Doney, S. (1994). Oceanic vertical mixing: A review and a model with nonlocal boundary layer parameterization. *Reviews of Geophysics*, *32*, 363–403.

Levine, R. C., Turner, A. G., Marathayil, D., & Martin, G. M. (2013). The role of northern Arabian Sea surface temperature biases in CMIP5 model simulations and future projections of Indian summer monsoon rainfall. *Climate Dynamics*, *41*, 155–172. https://doi.org/10.1007/s00382-012-1656-x

Lozovatsky, I., Roget, E., Fernando, H., Figueroa, M., & Shapovalov, S. (2006). Sheared turbulence in a weakly stratified upper ocean. *Deep Sea Research, Part I*, *53*(2), 387–407. https://doi.org/10.1175/2010JPO44557.1

Lucas, A. J., Nash, J. D., Pinkel, R., MacKinnon, J. A., Tandon, A., Mahadevan, A., et al. (2016). Adrift upon a salinity-stratified sea: A view of upper-ocean processes in the Bay of Bengal during the southwest monsoon. *Oceanography*, *29*(2), 134–145. https://doi.org/10.5670/oceanog.2016.46

Maritorena, S., d'Andon, O. H. F., Mangin, A., & Siegel, D. A. (2010). Merged satellite ocean color data products using a bio-optical model: Characteristics, benefits and issues. *Remote Sensing of Environment*, *114*(8), 1791–1804. https://doi.org/10.1016/j.rse.2010.04.002

McPhaden, M. J. (1982). Variability in the central equatorial Indian Ocean, part II: Oceanic heat and turbulent energy balance. *Journal of Marine Research*, *40*, 403–419.

McPhaden, M. J., Meyers, G., Ando, K., Masumoto, Y., Murty, V. S. N., Ravichandran, M., et al. (2009). RAMA, the research moored array for African–Asian–Australian monsoon analysis and prediction: A new moored buoy array in the historically data-sparse Indian Ocean provides measurements to advance monsoon research and forecasting. *Bulletin of the American Meteorological Society*, *90*, 459–480. https://doi.org/10.1175/2008BAMS2608.1

Moisin, J. R., & Niiler, P. P. (1998). The seasonal heat budget of the North Pacific: Net heat flux and heat storage rates (1950–1990). *Journal of Physical Oceanography*, *28*, 401–421.

Morel, A., & Antoine, D. (1994). Heating rate within the upper ocean in relation to its bio-optical state. *Journal of Physical Oceanography*, *24*, 1652–1665. https://doi.org/10.1175/1520-0485(1994)024<1652:HRWTUO>2.0.CO;2

Moum, J. N., Perlin, A., Nash, J. D., & McPhaden, M. J. (2013). Seasonal sea surface cooling in the equatorial Pacific cold tongue controlled by ocean mixing. *Nature*, *500*(7460), 64–67. https://doi.org/10.1038/nature12363

Moum, J. N., & Smyth, W. D. (2001). Upper ocean mixing processes. In J. H. Steele, K. K. Turekina, & S. A. Thorpe (Eds.), *Encyclopedia of ocean sciences* (Vol. 6, pp. 291–298). New York, ISBN 0–12–227430-x: Elsevier. https://doi.org/10.1006/rwos.2001

Nachar, N. (2008). The Mann-Whitney *U*: A test for assessing whether two independent samples come from the same distribution. *Tutorial in Quantitative Methods for Psychology*, *4*(1), 13–20.

Pant, V., Girishkumar, M. S., UdayaBhaskar, T. V. S., Ravichandran, M., Papa, F., & Thangaprakash, V. P. (2015). Observed interannual variability of near-surface salinity in the Bay of Bengal. *Journal of Geophysical Research, Oceans*, *120*, 3315–3329. https://doi.org/10.1002/2014JC010340

Pokhrel, S., Rahaman, H., Parekh, A., Saha, S. K., Dhakate, A., Chaudhari, H. S., & Gairola, R. M. (2012). Evaporation-precipitation variability over Indian Ocean and its assessment in NCEP Climate Forecast System (CFSv2). *Climate Dynamics*, *39*, 2585–2608.

Prasad, T. G. (2004). A comparison of mixed-layer dynamics between the Arabian Sea and Bay of Bengal: One-dimensional model results. *Journal of Geophysical Research*, *109*, C03035. https://doi.org/10.1029/2003JC002000

Praveen Kumar, B., Vialard, J., Lengaigne, M., Murty, V. S. N., & McPhaden, M. J. (2012). TropFlux: Air-sea fluxes for the global tropical oceans—Description and evaluation. *Climate Dynamics*, *38*, 1521–1543. https://doi.org/10.1007/s00382-011-1115-0

Rao, R. R., & Sivakumar, R. (2000). Seasonal variability of near-surface thermal structure and heat budget of the mixed layer of the tropical Indian Ocean from a new global ocean temperature climatology. *Journal of Geophysical Research*, *105*(C1), 995–1015. https://doi.org/10.1029/1999JC900220

Rao, R. R., & Sivakumar, R. (2003). Seasonal variability of sea surface salinity and salt budget of the mixed layer of the north Indian Ocean. *Journal of Geophysical Research*, *108*(C1), 3009. https://doi.org/10.1029/2001JC000907

Ricciardulli, L., & Wentz, F. J. (2016). *Remote sensing systems ASCAT C-2015 daily ocean vector winds on 0.25 deg grid, version 2.1*. Santa Rosa, CA: Remote sensing systems.

Scannell, H. A., & McPhaden, M. J. (2018). Seasonal mixed layer temperature balance in the southeastern tropical Atlantic. *Journal of Geophysical Research: Oceans*, *123*, 5557–5570. https://doi.org/10.1029/2018JC014099

Sengupta, D., Ray, P. K., & Bhat, G. S. (2002). Spring warming of the eastern Arabian Sea and Bay of Bengal from buoy data. *Geophysical Research Letters*, *29*(15), 24–1. https://doi.org/10.1029/2002GL015340

Seo, H., Xie, S., Murtugudde, R., Jochum, M., & Miller, A. J. (2009). Seasonal effects of Indian Ocean freshwater forcing in a regional coupled model. *Journal of Climate*, *22*, 6577–6596. https://doi.org/10.1175/2009JCLI2990.1

Shankar, D., Vinayachandran, P. N., & Unnikrishnan, A. S. (2002). The monsoon currents in the North Indian Ocean. *Progress in Oceanography*, *52*(1), 63–120.

Shenoi, S. S. C., Shankar, D., & Shetye, S. R. (2002). Differences in heat budgets of the near-surface Arabian Sea and Bay of Bengal: Implications for the summer monsoon. *Journal of Geophysical Research*, *107*(C6), 3052. https://doi.org/10.1029/2000JC000679

Shroyer, E. L., Rudnick, D. L., Farrar, J. T., Lim, B., Venayagamoorthy, S. K., St. Laurent, L. C., et al. (2016). Modification of upper-ocean temperature structure by subsurface mixing in the presence of strong salinity stratification. *Oceanography*, *29*(2), 62–71. https://doi.org/10.5670/oceanog.2016.39

Sun, O. M., Jayne, S. R., Polzin, K. L., Rahter, B. A., & Laurent, L. C. S. (2013). Scaling turbulent dissipation in the transition layer. *Journal of Physical Oceanography*, *43*, 2475–2489. https://doi.org/10.1175/JPO-D-13-057-1

Sweers, H. E. (1970). Vertical diffusivity coefficient in a thermocline. *Limnology and Oceanography*, *15*, 273–280.

Thadathil, P., Gopalakrishna, V. V., Muraleedharan, P. M., Reddy, G. V., Araligidad, N., & Shenoy, S. S. C. (2002). Surface layer temperature inversion in the Bay of Bengal. *Deep Sea Research, Part I*, *49*, 1801–1818. https://doi.org/10.1016/S0967-0637(02)00044-4

Thadathil, P., Muraleedharan, P. M., Rao, R. R., Somayajulu, Y. K., Reddy, G. V., & Revichandran, C. (2007). Observed seasonal variability of barrier layer in the Bay of Bengal. *Journal of Geophysical Research*, *112*, C02009. https://doi.org/10.1029/2006JC003651

Thadathil, P., Suresh, I., Gautham, S., Prasanna Kumar, S., Lengaigne, M., Rao, R. R., et al. (2016). Surface layer temperature inversion in the Bay of Bengal: Characteristics and related mechanisms. *Journal of Geophysical Research, Oceans*, *121*, 5682–5696. https://doi.org/10.1002/2016JC011674

Thakur, R., Shroyer, E. L., Govindarajan, R., Farrar, J. T., Weller, R. A., & Moum, J. N. (2019). Seasonality and buoyancy suppression of turbulence in the Bay of Bengal. *Geophysical Research Letters*, *46*, 4346–4355. https://doi.org/10.1029/2018GL081577

Thangaprakash, V. P., Girishkumar, M. S., Suprit, K., Suresh Kumar, N., Chaudhuri, D., Dinesh, K., et al. (2016). What controls seasonal evolution of sea surface temperature in the Bay of Bengal? Mixed layer heat budget analysis using moored buoy observations along 90°E. *Oceanography*, *29*(2), 202–213. https://doi.org/10.5670/oceanog.2016.52

Thomson, R. E., & Emery, W. J. (2014). Data analysis methods in physical oceanography. In R. E. Thomson, & W. J. Emery (Eds.), *Chapter 3—Statistical methods and error handling*, (third ed., Vol. 2014, pp. 219–311, ISBN 9780123877826)., Boston, Massachusetts: Elsevier. https://doi.org/10.1016/B978-0-12-387782-6.00003-X

Varkey, M. J., Murty, V. S. N., & Suryanarayana, A. (1996). Physical oceanography of the Bay of Bengal and Andaman Sea. In A. D. Ansell, et al. (Eds.), *Oceanography and marine biology: An annual review*, (Vol. 34, pp. 1–70). London: Univ. Coll. of London Press.

Wade, M., Caniaux, G., & du Penhoat, Y. (2011). Variability of the mixed layer heat budget in the eastern equatorial Atlantic during 2005–2007 as inferred using Argo floats. *Journal of Geophysical Research*, *116*, C08006. https://doi.org/10.1029/2010JC006683

Wang, W., & McPhaden, M. J. (1999). The surface-layer heat balance in the equatorial Pacific Ocean. Part I: Mean seasonal cycle. *Journal of Physical Oceanography*, *29*, 1812–1831. https://doi.org/10.1175/1520-0485(1999)029%3C1812:TSLHBI%3E2.0.CO;2

Warner, S. J., Becherer, J., Pujiana, K., Shroyer, E. L., Ravichandran, M., Thangaprakash, V. P., & Moum, J. N. (2016). Monsoon mixing cycles in the Bay of Bengal: A year-long subsurface mixing record. *Oceanography*, *29*(2), 158–169. https://doi.org/10.5670/oceanog.2016.48

Yu, L., Jin, X. & Weller, R. A. (2008). Multidecade global flux datasets from the Objectively Analyzed Air-Sea Fluxes (OAFlux) project: Latent and sensible heat fluxes, ocean evaporation, and related surface meteorological variables. Woods Hole Oceanographic Institution, OAFlux project technical report. OA-2008-01, 64pp. Woods hole. Massachusetts

Yu, Z. H., Tian-Jun, Z., & Li-Wei, Z. (2012). Indian Ocean SST biases in a flexible regional ocean atmosphere land system (FROALS) model. *Atmospheric and Oceanic Science Letters*, *5*(4), 273–279. https://doi.org/10.1080/16742834.2012.11447012